2016

Unique epigenetic influence of H2AX phosphorylation and H3K56 acetylation on normal stem cell radioresponses

Keith M. Jacobs
Washington University School of Medicine

Sandeep Misri
Washington University School of Medicine

Barbara Meyer
Washington University School of Medicine

Suyash Raj
Washington University School of Medicine

Cheri L. Zobel
Washington University School of Medicine

See next page for additional authors

Authors
Keith M. Jacobs, Sandeep Misri, Barbara Meyer, Suyash Raj, Cheri L. Zobel, Barry P. Sleckman, Dennis E. Hallahan, and Girdhar G. Sharma

Unique epigenetic influence of H2AX phosphorylation and H3K56 acetylation on normal stem cell radioresponses

Keith M. Jacobs[a], Sandeep Misri[a], Barbara Meyer[a], Suyash Raj[a], Cheri L. Zobel[a], Barry P. Sleckman[b,c,†], Dennis E. Hallahan[a,b], and Girdhar G. Sharma[a,b,*]

[a]Department of Radiation Oncology, Cancer Biology Division, [b]Siteman Cancer Center, and [c]Department of Pathology, Laboratory and Genomic Medicine, Washington University School of Medicine, St. Louis, MO 63108

ABSTRACT **Normal tissue injury resulting from cancer radiotherapy is often associated with diminished regenerative capacity. We examined the relative radiosensitivity of normal stem cell populations compared with non–stem cells within several radiosensitive tissue niches and culture models. We found that these stem cells are highly radiosensitive, in contrast to their isogenic differentiated progeny. Of interest, they also exhibited a uniquely attenuated DNA damage response (DDR) and muted DNA repair. Whereas stem cells exhibit reduced ATM activation and ionizing radiation–induced foci, they display apoptotic pannuclear H2AX-S139 phosphorylation (γH2AX), indicating unique radioresponses. We also observed persistent phosphorylation of H2AX-Y142 along the DNA breaks in stem cells, which promotes apoptosis while inhibiting DDR signaling. In addition, down-regulation of constitutively elevated histone-3 lysine-56 acetylation (H3K56ac) in stem cells significantly decreased their radiosensitivity, restored DDR function, and increased survival, signifying its role as a key contributor to stem cell radiosensitivity. These results establish that unique epigenetic landscapes affect cellular heterogeneity in radiosensitivity and demonstrate the nonubiquitous nature of radiation responses. We thus elucidate novel epigenetic rheostats that promote ionizing radiation hypersensitivity in various normal stem cell populations, identifying potential molecular targets for pharmacological radioprotection of stem cells and hopefully improving the efficacy of future cancer treatment.**

Monitoring Editor
A. Gregory Matera
University of North Carolina

Received: Jan 12, 2016
Accepted: Feb 22, 2016

INTRODUCTION

Radiation therapy uses ionizing radiation (IR) to produce lethal DNA double-strand breaks (DSBs) in cancer cells. Unfortunately, unintended damage to normal tissue often results in detrimental clinical consequences (Greenberger, 2009), such as cognitive impairment (Duffner, 2004), infertility (Ash, 1980), intestinal epithelial erosion (Smith and DeCosse, 1986), and embryonic/fetal lethality (Martin, 2011). The underlying cause of these sequelae has been attributed to the IR-induced dysfunction of regenerative stem cell compartments (Hellman and Botnick, 1977), but the mechanistic details of normal stem cell radiosensitivity remain unclear. An improved understanding of stem cell–specific differential radiation responses is essential for the development of therapeutic strategies to protect normal tissue during radiotherapy.

The DNA damage response (DDR) is an intricate network of molecular signaling after induction of DSBs that initiates damage sensing, activation and recruitment of repair factors, chromatin alterations, and DNA repair. Aberrant DDR signaling often leads to genomic instability and cell death (Jackson and Bartek, 2009), suggesting that diminished DDR signaling and DNA repair capacity may contribute to radiation hypersensitivity. The DDR is strongly

This article was published online ahead of print in MBoC in Press (http://www.molbiolcell.org/cgi/doi/10.1091/mbc.E16-01-0017) on March 3, 2016.

†Present address: Department of Pathology and Laboratory Medicine, Weill Cornell Medical College, New York, NY 10065.

K.M.J. performed most DDR and histone experiments, and S.M. performed most apoptosis experiments. B.M., S.R., and C.L.Z. did various experiments. B.P.S., D.E.H., and G.G.S. aided with inputs and interpretations. K.M.J., B.M., and G.G.S. wrote the article. G.G.S. conceived of and directed the work.

*Address correspondence to: Girdhar G. Sharma (sharma@wustl.edu).

Abbreviations used: DDR, DNA damage response; DSB, DNA double-strand break; H3K56ac, histone-3 lysine-56 acetylation; IR, ionizing radiation; IRIF, ionizing radiation–induced foci.

Supplemental Material can be found at:
http://www.molbiolcell.org/content/suppl/2016/02/29/mbc.E16-01-0017v1.DC1.html

influenced by the chromatin configuration around DSBs and associated regulation of various histone modifications (Lukas *et al.*, 2011). Chromatin modifications can potentially control access of repair factors to DNA and may therefore have a substantial influence on cellular radiation response outcomes, leading to differential radiosensitivities.

Here we determine that multiple populations of normal stem cells, both in vivo and in culture from tissues often exhibiting radiation injury, are hypersensitive to IR, in contrast with their directly differentiated isogenic progeny. We demonstrate that these stem cells exhibit a severely attenuated DDR and diminished DNA repair efficacy, corresponding to a starkly reduced DNA damage threshold for inducing IR-induced cell death. We also elucidate novel epigenetic regulation of these radiation responses in stem cells, including apoptotic pan-γH2AX, failure to dephosphorylate H2AX Y142 after DNA damage, and constitutively elevated histone-3 lysine-56 acetylation (H3K56ac) at DNA break sites. Downregulation of H3K56ac significantly protected stem cells from IR-induced apoptosis and improved DDR signaling, substantiating the mechanistic associations between chromatin organization, epigenetic regulation, and radiosensitivity. These histone modifications may therefore serve as potential therapeutic targets for targeted protection of normal tissue during radiotherapy, advancing more effective radiation treatment and improved patient outcomes.

RESULTS

Normal stem cells are radiation hypersensitive

Clinical consequences from irradiation of proliferative tissues have been attributed to stem cell dysfunction. We therefore examined whether stem cells within some of these tissues exhibited increased radiosensitivity. We analyzed IR-induced apoptosis in brain, testis, and intestine by staining for common apoptotic markers after whole-body irradiation of C57BL/6 young adult male mice. A panel of known stem cell markers (Fox *et al.*, 1983; Pesce *et al.*, 1998; Suh *et al.*, 2007) was used to identify stem cell populations within each tissue. At lower IR doses (2–6 Gy) apoptosis was both exclusive to and highly prevalent among various stem cell populations within all studied tissue niches (Figure 1, A and C, and Supplemental Figure S1A), whereas stem cell death was not observed in unirradiated samples (Figure 1C and Supplemental Figure S1B). In contrast, differentiated (non-stem) cells were highly radioresistant and only underwent minimal apoptosis even at higher doses (8–10 Gy; Figure 1, A–C), indicating that stem cells exhibit a markedly lower DNA damage threshold for IR-induced apoptosis.

We also established early-passage, primary culture models of murine embryonic stem (ES) and neural stem (NS) cells, avoiding prolonged passages to minimize potential culture artifacts (Diaz Perez *et al.*, 2012). We confirmed isogenic differentiation of both cell types (ES to ED and NS to ND) by a panel of pluripotency markers corresponding with marked morphological changes (Supplemental Figure S1, C and D). We observed that stem cell–specific apoptosis was recapitulated in both culture model sets after 6-Gy IR, with stem cells displaying radiosensitivity and non–stem cells exhibiting strong radioresistance (Figure 1D and Supplemental Figure S1E). Of note, ES and ED cells in culture demonstrated comparable cell cycle progression (Supplemental Figure S1F), indicating that increased radiosensitivity in stem cells is not merely due to rapid proliferation. Whereas progressive reduction in comet assay olive moment signified repair of DNA breaks in differentiated cells, stark increase in stem cell olive moment at later time points indicated apoptotic DNA fragmentation (Figure 1E). Furthermore, clonogenic survival analyses confirmed substantially higher rates of IR-induced cell killing and radiosensitivity in cultured stem cells (Figure 1F). The apoptotic markers of cleaved poly(ADP-ribose) polymerase (PARP) and cleaved caspase-3 were also detected exclusively in stem cells beginning at 4-h postirradiation. In addition, levels of proapoptotic Bax were higher and IR induced in stem cells, whereas the antiapoptotic Bcl-2 was elevated in non–stem cells (Figure 1G). Therefore these undifferentiated stem cell populations from in vivo tissue niches as well as in culture are substantially radiosensitive and readily undergo IR-induced programmed cell death, in contrast with the isogenic differentiated non–stem cells.

Stem cells exhibit an attenuated DDR

We investigated whether differential radiosensitivity among these populations of stem cells and non–stem cells was associated with any significant differences in the DDR. DDR signaling begins with the Mre11–Rad50–NBS1 (MRN) complex initially sensing DNA breaks (Lee and Paull, 2007). This is followed by activation of phosphatidylinositol 3-kinase–related kinases, which include ataxia telangiectasia mutated (ATM), ATM and Rad3-related (ATR), and DNA-dependent protein kinase catalytic subunit (DNA-PKcs) (Jackson and Bartek, 2009). Activated ATM phosphorylates histone H2AX on serine 139, marking megabases of chromatin around the DSB with γH2AX (Burma *et al.*, 2001), which serves as a docking site for downstream repair factors (Paull *et al.*, 2000). Our careful investigation of stem cell niches in vivo revealed cells noticeably devoid of γH2AX IR-induced foci (IRIF) specifically in the stem cell region of these tissues (Figure 2A, left). On costaining with stem cell markers, we observed that these remarkably diminished γH2AX IRIF occurred within the majority of stem cells in all tissues surveyed minutes after irradiation, whereas surrounding non–stem cells displayed robust γH2AX signals (Figure 2, A, right, and B, and Supplemental Figure S2A). IRIF were not seen in unirradiated controls (Supplemental Figure S2B). A similarly attenuated DDR was also observed in tissues at 1-h postirradiation (Supplemental Figure S2C), implying that foci induction is not merely delayed. Stem cells in culture also exhibited strongly attenuated IR induction of γH2AX both globally by immunoblots (Figure 2C) and locally along microirradiation tracks (Figure 2D and Supplemental Figure S3A). Total H2AX levels were similar among the cell types and were unchanged after irradiation (Figure 2C and Supplemental Figure S3B). ATM activation (S1981 phosphorylation) and its recruitment to DSBs were markedly reduced in ES cells in culture (Figure 2, E and F), as well as in vivo within subgranular zone (SGZ) stem cells of brain after irradiation (Supplemental Figure S3C). ES cells also demonstrated reduced ATR activation (S1989 and Chk1 S345 phosphorylation; Supplemental Figure S3D).

DNA DSB repair occurs through either nonhomologous end joining (NHEJ) or homologous recombination (HR). Stem cells failed to recruit activated NHEJ repair factor DNA-PKcs (S2056 phosphorylation) to DSBs in culture (Figure 2G). Of interest, at higher doses (10 Gy), we were also able to visualize pDNA-PK in the SGZ of brain, with foci predominantly confined to differentiated cells (Supplemental Figure S4A). Rad51 foci indicative of HR were also selectively absent from irradiated stem cells in vivo after 10-Gy irradiation (Supplemental Figure S4B). Together these data clearly demonstrate that radiosensitive stem cells both in these tissues and in culture exhibit an abrogated DDR.

IR-induced apoptosis typically involves DDR signaling through ATM (Norbury and Zhivotovsky, 2004); however, DNA damage–induced apoptosis in stem cells has been shown to be uniquely ATM independent (Lee *et al.*, 2001). It was therefore interesting that the neural stem cell niche of mice lacking or defective in ATM, DNA-PK,

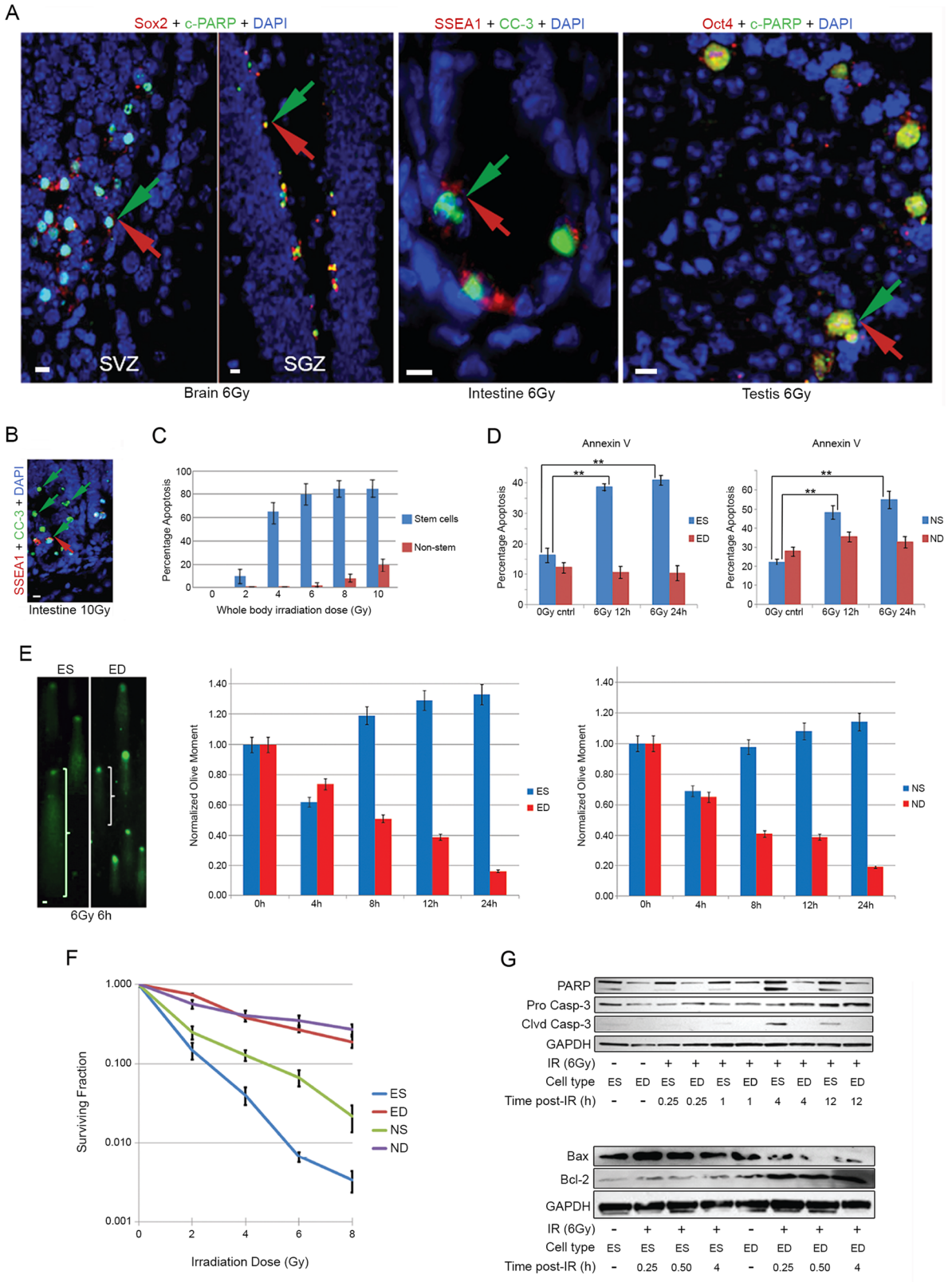

FIGURE 1: Stem cells demonstrate increased radiosensitivity. (A) Costaining of Sox2 (red) and cleaved PARP (c-PARP, green) in brain, SSEA1 (red) and cleaved caspase-3 (CC-3, green) in intestine, and Oct4 (red) and c-PARP (green) in testis 12 h after 6-Gy IR. SGZ, subgranular zone; SVZ, subventricular zone. Punctate staining is due to nuclear fragmentation upon apoptosis; 25 sections across five different mice. Magnification: SVZ, intestine, testis, 63×; SGZ, 20×. (B) Costaining of SSEA1 (red) and CC-3 (green) in intestine 12 h after 10-Gy IR. Ten sections across three different mice. Magnification, 20×. (C) Quantification of apoptotic stem cells and non–stem cells 12 h after various IR doses. Approximately 300 cells were scored across several crypts. $N = 5$ sections. (D) Flow cytometric analysis of apoptosis comparing ES and ED or NS

or H2AX function still underwent IR-induced apoptosis (Supplemental Figure S4C), indicating that IR-induced apoptosis in stem cells may exhibit uniquely alternative signaling.

Stem cells fail to effectively repair DSBs

We then investigated potential differences in DNA repair proficiency between stem and differentiated cells. A dose of 2 Gy was used because higher doses blocked cell cycle progression into mitosis and greatly diminished the yield of mitotic cells. Non–stem cells exhibited efficient repair, as indicated by rapid reduction of DNA breaks (Figure 3A). Stem cells, in contrast, exhibited reduced repair efficiency, failing to show substantial DNA repair until 4 h post-IR, when many of the radiosensitive cells had likely begun dropping out of the population through apoptosis (Figure 1, E and G). Stem cells also displayed significantly higher incidences of residual chromosome and chromatid breaks after IR, as well as noticeably abundant nuclear fragmentation (Figure 3, B and C), whereas only minimal aberrations were seen in non–stem cells or unirradiated controls (Figure 3C and Supplemental Figure S4D). Intriguingly, despite the attenuated downstream DDR signaling, we observed normal recruitment of the DNA damage "sensor" NBS1 (Nibrin), a component of the MRN complex (Figure 3D), along with the early DSB responder Ku80 (Supplemental Figure S4E) to the break sites in stem cells. Although it is part of the DNA-PK complex, the Ku70/80 heterodimer is an early responder to DSBs that does not require DNA-PKcs for its recruitment at DSBs (Koike and Koike, 2008). The presence of these complexes at DSBs in stem cells suggests a disconnect between initial DSB sensing and downstream signal transduction, resulting in deficient recruitment/retention of repair factors and muted DNA repair. Attenuation of the DDR in these stem cells thus leads to reduced DNA repair efficiency and likely explains their reduced threshold for DNA damage–induced apoptosis.

IR-induced apoptosis in stem cells involves the MST1-JNK-H2AX pathway and is associated with a lack of H2AX-Y142 dephosphorylation

Despite the absence of γH2AX IRIF in stem cells in vivo soon after irradiation (Figure 2, A and B), by 6 h postirradiation, we were surprised to observe pannuclear γH2AX (pan-γH2AX) in these cells (Figure 4A and Supplemental Figure S5A). Once activated after apoptotic stimuli by caspase cleavage (Wen *et al.*, 2010), autophosphorylation (Praskova *et al.*, 2004), and subsequent nuclear translocation, mammalian Ste20-like kinase (MST1) pan-phosphorylates H2AX (at the same S139 site targeted by ATM). MST1 also activates JNK (c-jun N-terminal kinase) (Ura *et al.*, 2007), which can itself pan-phosphorylate H2AX (Lu *et al.*, 2006). In addition, MST1 has been shown to promote apoptosis upstream of caspase cleavage through inhibition of Bcl-xL (Del Re *et al.*, 2014). We therefore investigated whether MST1 and JNK activation was associated with apoptotic pan-γH2AX in stem cells. MST1 was phosphorylated (T183) only in stem cells after irradiation (Figure 4B), and pan-γH2AX colocalized with nuclear translocation of otherwise cytoplasmic MST1 in the SGZ at late time points (Figure 4C). In addition, JNK was activated (T183/Y185 phosphorylation) only in stem cells at late time points after irradiation both in culture (Figure 4B) and in vivo (Figure 4D and Supplemental Figure S5B). pJNK also costained with pan-γH2AX (Figure 4E) in the SGZ stem cell region.

Tyrosine 142 of histone H2AX is constitutively phosphorylated by WSTF kinase (H2AX-pY142), but dephosphorylation by EYA phosphatase upon DNA damage is required for recruitment of mediator of DNA damage checkpoint protein 1 (MDC1) to γH2AX and downstream DDR signaling (Cook *et al.*, 2009; Xiao *et al.*, 2009). Failure to dephosphorylate H2AX-pY142 blocks DDR signaling and promotes apoptosis through JNK activation/recruitment, which we observed in stem cells. We thus examined whether the distinctive radiation responses of stem cells involve unique regulation of H2AX-pY142. H2AX-pY142 was mutually exclusive from γH2AX-labeled microirradiation tracks of DNA damage in differentiated culture cells, whereas H2AX-pY142 persisted in stem cells where γH2AX was abrogated (Figure 4F and Supplemental Figure S5C). Immunoblotting also confirmed that Y142 was dephosphorylated only in non–stem cells after irradiation (Figure 4G). In addition, MDC1 was not recruited to DSBs (Supplemental Figure S5D) and H2AX-pY142 was absent from MDC1-labeled tracks only in non–stem cells (Figure 4H). The persistence of constitutive H2AX-pY142 after DNA damage in stem cells may promote apoptosis while hindering the DDR.

Constitutively elevated H3K56ac in stem cells negatively correlates with DDR induction

H3K56ac has been implicated as a DNA damage–responsive histone modification (Das *et al.*, 2009; Tjeertes *et al.*, 2009; Miller *et al.*, 2010; Vempati *et al.*, 2010) and is directly involved in maintaining the pluripotent state of ES cells (Xie *et al.*, 2009). We therefore examined the connection between H3K56ac levels and DDR in stem cells. We observed dramatically enhanced levels of H3K56ac in the inner cell mass of blastocyst-stage embryos where ES cells originate (Figure 5A), and high H3K56ac levels in cultured ES cells sharply decreased upon differentiation (Figure 5B). Of interest, elevated H3K56ac was associated with an absence of IRIFs after irradiation of coplated ES and ED cells (Figure 5C), and high H3K56ac levels in stem cell regions in vivo also corresponded to diminished IRIF (Figure 5D).

H3K56ac was significantly reduced along γH2AX-labeled DSBs at very early time points (<10 min) after DNA damage only in ED cells, whereas H3K56ac was unchanged in ES cells (Figure 6, A and B). H3K56ac reduction along break sites in non–stem cells was not due to eviction of histones from the break site (Supplemental Figure S6A) and was transient in nature, as H3K56ac reduction was not observed at later time points (Figure 6C). Constitutively elevated H3K56ac in stem cells may therefore be inhibitory for DDR signaling.

H3K56ac depletion imparts radioprotection to stem cells and restores the DDR

Expression of the H3K56ac acetyltransferase p300 (Das *et al.*, 2009) paralleled elevated H3K56ac levels in cultured stem cells and remained elevated after irradiation (Figure 7, A and B).

and ND cells by annexin V labeling after sham or 6-Gy IR at indicated time points. We counted 10,000 gated cells. $N = 3$; $^{**}p < 0.01$, otherwise not significant. (E) Olive moments of comet assay tails at different time points after 6-Gy IR normalized to the irradiated 0-min time point. From 50 to 75 comets/sample. $N = 3$. Representative comet tails 6 h after 6-Gy IR. Magnification, 20×. (F) Clonogenic survival after various IR doses. Colonies containing >50 cells were counted. $N = 3$. (G) Western blots for apoptotic effectors after mock or 6-Gy irradiation of ES and ED cells. Glyceraldehyde-3-phosphate dehydrogenase (GAPDH) is the loading control. CC-3, Clvd casp 3, cleaved caspase-3; Pro casp 3, Pro caspase-3. DAPI = DNA. Error bars indicate SEM. Scale bars, 10 µm. Representative images and blots.

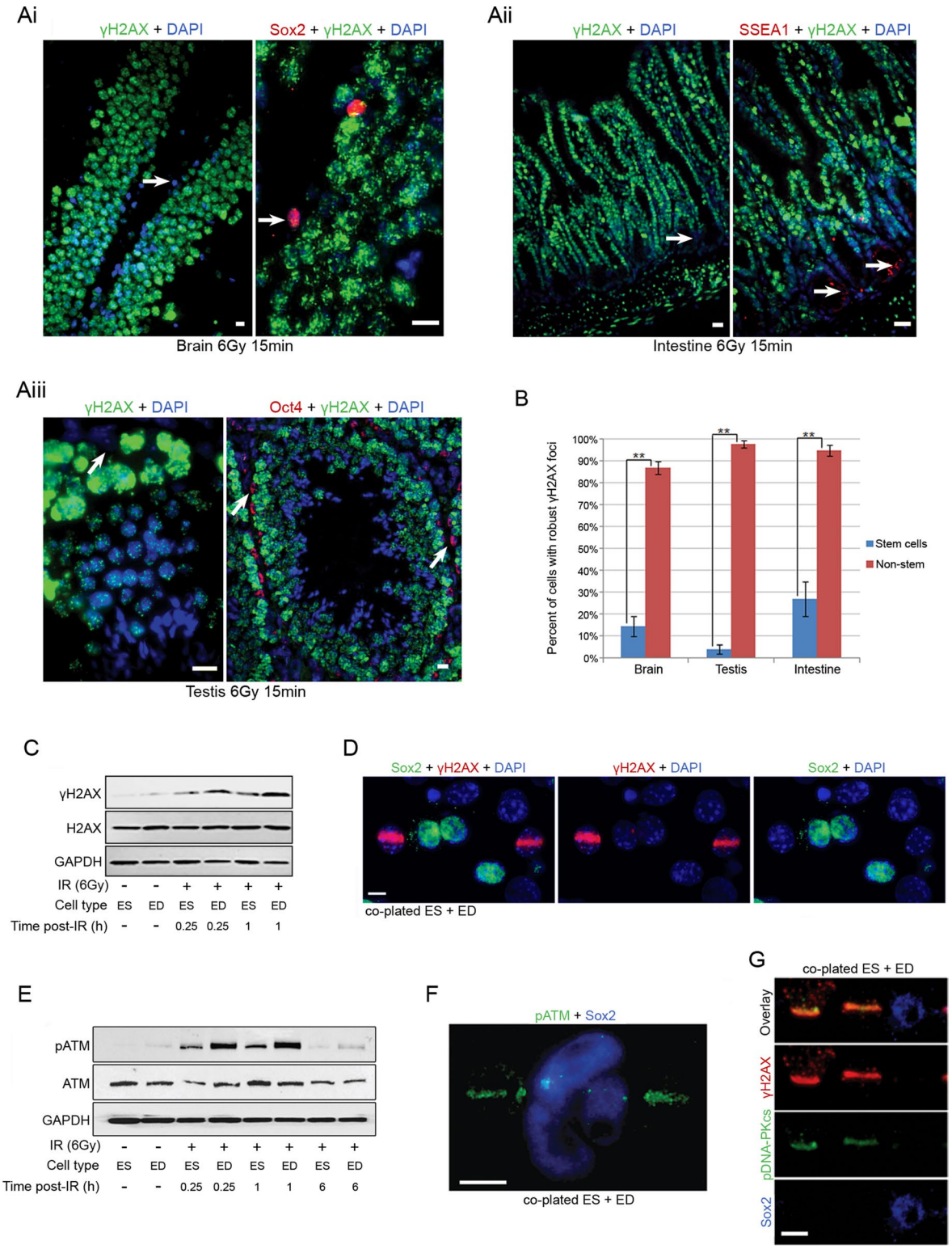

FIGURE 2: Stem cells exhibit an attenuated DDR. (A) Costaining of γH2AX (green) and stem cell marker (red) in (Ai) brain (Sox2), (Aii) intestine (SSEA1), and (Aiii) testis (Oct4) 15 min after 6-Gy IR. Arrows indicate stem cells lacking γH2AX. Magnification, 20× (left), 63× (right), reverse in testis. (B) Quantification of γH2AX-positive cells among stem cells and non–stem populations in three tissues. Approximately 250–300 cells were scored across multiple compartments for >2 bright foci/cell. $N = 20$ sections (each tissue) across four different mice; $^{**}p < 0.01$. Error bars indicate SEM. (C) Western blots for γH2AX and histone H2AX at various time points after mock or 6-Gy irradiation of ES and ED cells. GAPDH is loading control. (D) Costaining of Sox2 (green) and γH2AX (red) on coplated ES and ED cells after microirradiation. $N = 100$. Magnification, 63×. (E) Western blots for pATM (S1981) and total ATM after mock or 6-Gy irradiation of ES and ED cells. GAPDH is loading control. (F) Costaining of Sox2 (blue) and pATM (green) on

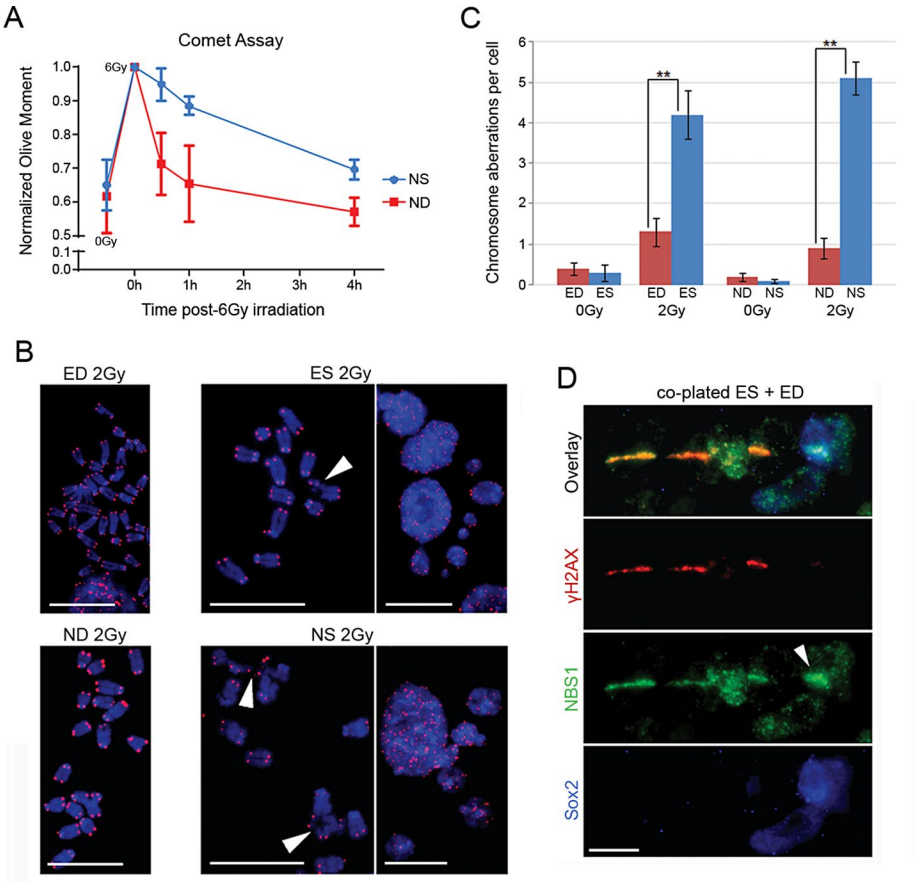

FIGURE 3: DNA repair proficiency is reduced in stem cells. (A) Olive moments of comet assay tails at different time points from NS and ND cells after sham or 6-Gy IR normalized to the irradiated 0-min time point. From 50 to 75 comets were scored per sample. $N = 3$. ANCOVA for the entire curve, $p = 0.023$. (B) Cytogenetic analysis of chromosome and chromatid breaks along with fragmented nuclei after 6-Gy IR. Red, telomere. Arrowheads indicate chromosome aberrations (breaks and radials). Magnification, 100×. (C) Quantification of chromosome aberrations after 2-Gy or sham irradiation. More than 100 metaphase plates were scored per sample. $N = 3$; $^{**}p < 0.01$. (D) Costaining of Sox2 (blue), γH2AX (red), and NBS1 (green) on coplated ES and ED cells after microirradiation. $N = 25$. Arrowhead indicates the presence of NBS1 despite attenuated γH2AX. Magnification, 63×. Error bars indicate SEM. Scale bars, 10 μm. Representative images. Microirradiation results were consistently observed in at least 75% of experiments.

Transient small interfering RNA (siRNA) knockdown of p300 substantially reduced H3K56ac levels (Figure 7C and Supplemental Figure S7A) without any effect on overall histone H3 or H4 acetylation (Figure 7D). The bromodomain-targeting p300/CBP inhibitor I-CBP112 also produced a sharp decrease in H3K56ac (Figure 7E and Supplemental Figure S7B). We therefore investigated whether p300-mediated transient down-regulation of H3K56ac had any direct effect on stem cell radiation responses.

Both p300 knockdown and inhibition substantially reduced IR-induced apoptosis in stem cells without any significant effect on differentiated cells (Figure 8, A and B), indicating that elevated H3K56ac likely promotes stem cell IR hypersensitivity. p300 inhibition also increased the intensity of otherwise reduced γH2AX foci in stem cells after irradiation (Figure 8C), approaching levels comparable to those of uninhibited differentiated cells. Additionally, H3K56ac down-regulation in stem cells increased pATM and γH2AX induction after irradiation (Figure 8D) and significantly improved DNA repair proficiency (Figure 8E). Elevated H3K56ac levels therefore directly promote the attenuated DDR and resulting IR hypersensitivity in these stem cell populations, and targeted transient down-regulation of H3K56ac can protect these cells from IR-induced damage.

DISCUSSION

Our study examines the radiosensitivity of stem cells as compared with their differentiated progeny across several tissues often exhibiting normal tissue radiation injury. Although these findings might not be applicable to all stem cell populations across every tissue niche, as relative radioresistance of some stem cells has been reported in other tissues (Sotiropoulou *et al.*, 2010; Sugrue *et al.*, 2013), our work clearly demonstrates that cellular populations within the niches studied here exhibit differentiation-dependent radiation responses that are regulated by concerted epigenetic and signaling mechanisms. We here establish that different cell types can vary in how they respond to DNA damage, testing existing assumptions concerning the ubiquitous nature of the DDR. The DDR, epigenetic, and radiosensitivity factors investigated in this study are summarized in Table 1.

Despite several studies demonstrating strong radiosensitivity of ES and NS cells (Acharya *et al.*, 2010; Zou *et al.*, 2012; Liu *et al.*, 2013), conflicting data exist reporting DDR activation and elevated repair factor expression (Chuykin *et al.*, 2008; Acharya *et al.*, 2010; Schneider *et al.*, 2011), as well as efficient repair of individual DSBs (Adams *et al.*, 2010; Tichy *et al.*, 2010) in cultured stem cells. Our data concede the occurrence of some level of DNA repair (albeit significantly diminished) in cultured stem cells. These stem cells were able to sense DNA breaks through MRN recruitment, which does not require γH2AX and is sufficient for promoting low levels of DNA repair (Celeste *et al.*, 2003; Yuan and Chen, 2010). Although this may be adequate for responding to endogenous low-level damage such as replicative errors and so on, these stem cells are incapable of repairing damage above a threshold (>2 Gy by our detection level). Therefore stem cells exhibiting elevated repair factor expression and the ability to repair individual

coplated ES and ED cells after microirradiation, N = 25. Magnification, 63×. (G) Costaining of Sox2 (blue), γH2AX (red), and pDNA-PKcs (S2056, green) on coplated ES and ED cells after microirradiation. $N = 15$. Magnification, 63×. Scale bars, 10 μm. Representative images and blots. Microirradiation results were consistently observed in at least 75% of experiments.

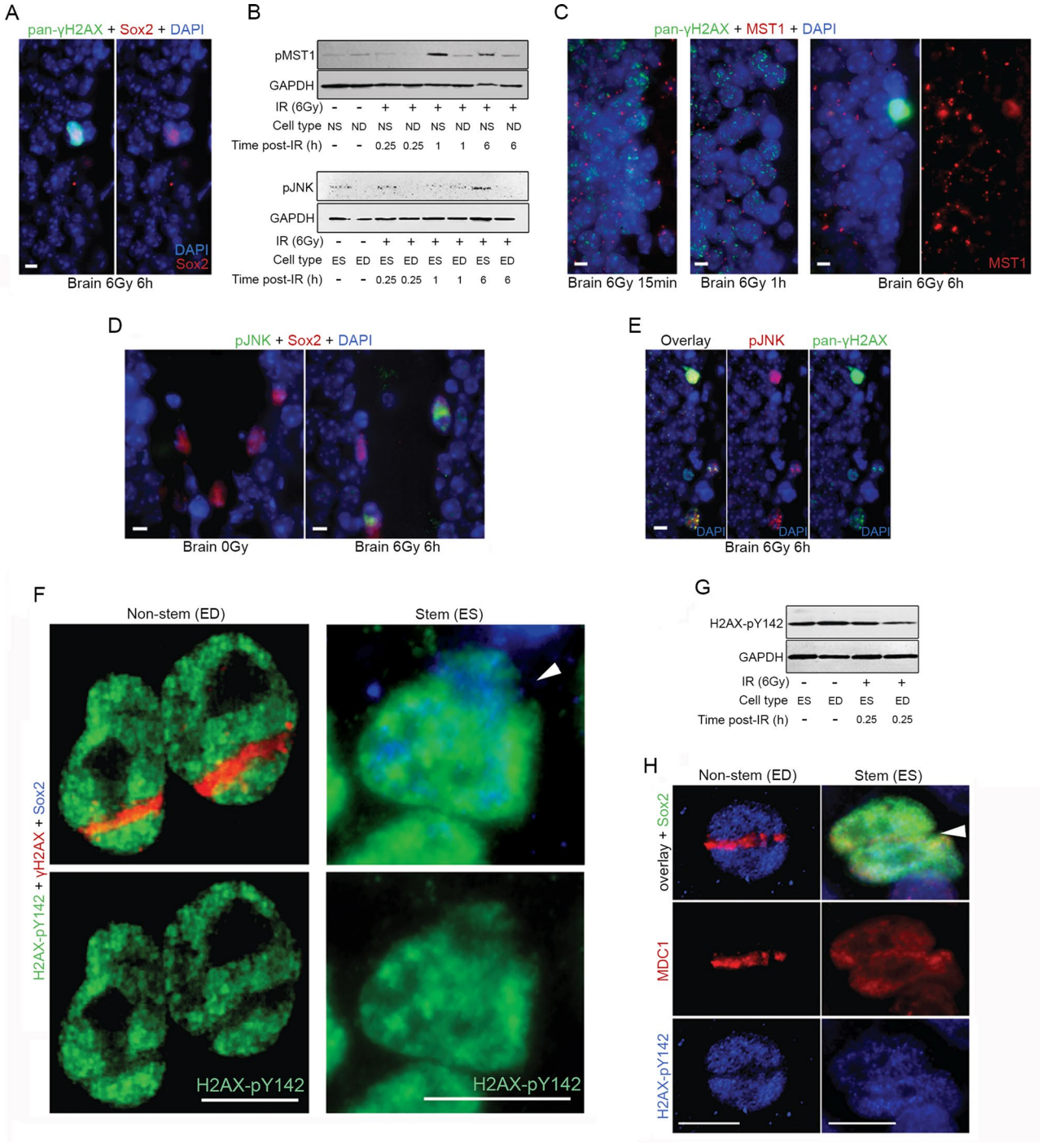

FIGURE 4: Stem cells activate the MST1-JNK-H2AX apoptosis pathway. (A) Costaining of Sox2 (red) and pan-γH2AX (green) in brain 6 h after 6Gy IR. *N* = 10 sections across three different mice. Magnification, 63×. (B) Western blots for pMST1 (T183) and pJNK (T183/Y185) at various time points after mock or 6-Gy irradiation of NS and ND cells or ES and ED cells, respectively. (C) Costaining of MST1 (red) and pan-γH2AX (green) in brain at 15 min, 1 h, and 6 h after 6-Gy IR. Ten sections across three different mice. Magnification, 63×. (D) Costaining of pJNK (green) and Sox2 (red) in brain 6 h after 6-Gy IR. Ten sections across three different mice. Magnification, 63×. (E) Costaining of pJNK (red) and pan-γH2AX (green) in brain 6 h after 6Gy IR. Ten sections across three different mice. Magnification, 63×. (F) Costaining of Sox2 (blue), γH2AX (red), and H2AX-pY142 (green) on coplated ES and ED cells after microirradiation. *N* = 50. Arrowhead marks the microirradiation path. Magnification, 63×. (G) Western blots for H2AX-pY142 after mock or 6-Gy irradiation of ES and ED cells. (H) Costaining of Sox2 (green), MDC1 (red), and H2AX-pY142 (blue) on coplated ES and ED cells after microirradiation. *N* = 25. Magnification, 63×. DAPI = DNA. GAPDH is loading control. Scale bars, 10 μm. Representative images and blots. Microirradiation results were consistently observed in at least 75% of experiments.

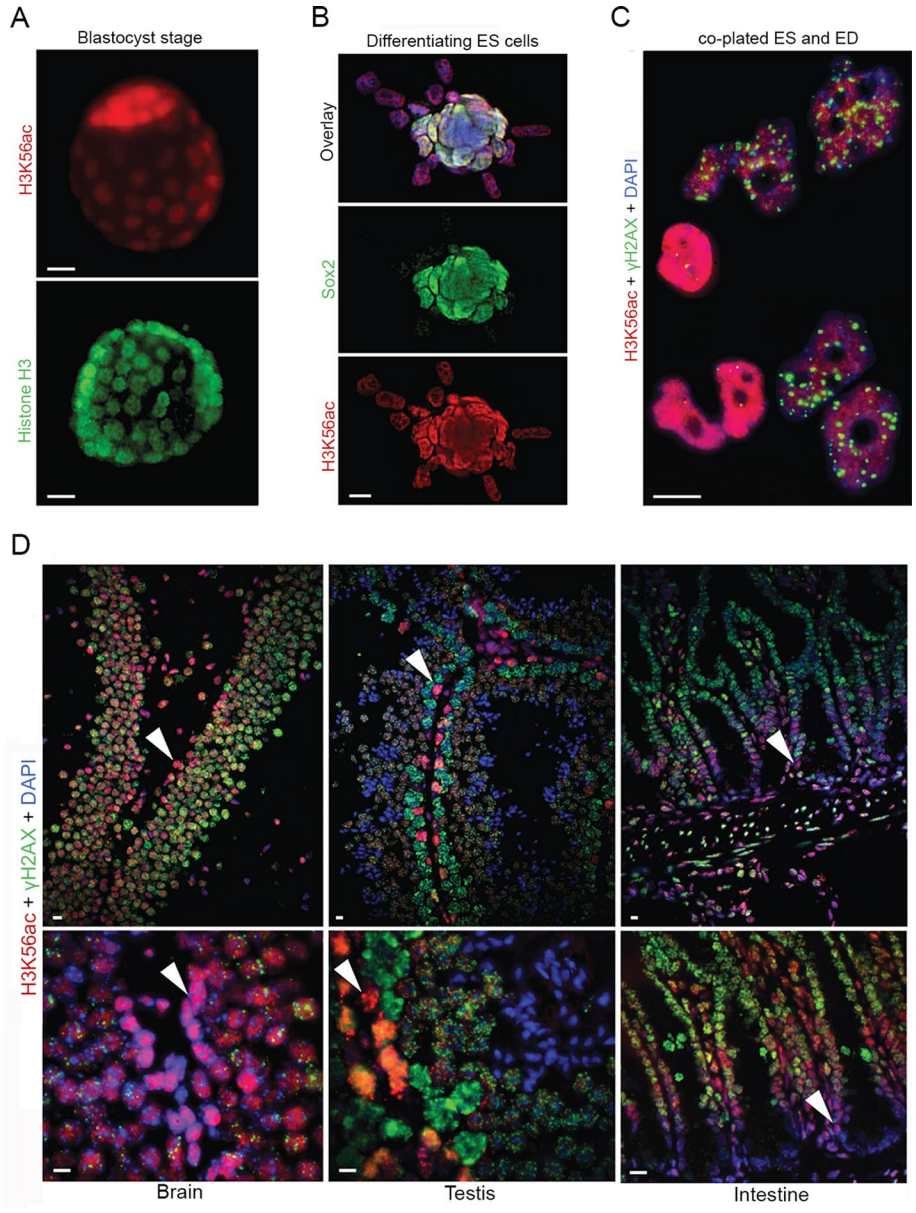

FIGURE 5: Elevated H3K56ac in stem cells is associated with abrogated IRIF. (A) Staining of H3K56ac (red) or total histone H3 (green) on unirradiated embryonic day 4.5 mouse embryos. Forty embryos. Magnification, 20×. (B) Costaining of Sox2 (green) and H3K56ac (red) on an unirradiated, differentiating ES cell colony; 15 colonies, three repetitions. Magnification, 20×. (C) Costaining of γH2AX (green) and H3K56ac (red) on coplated ES and ED cells 15 min after 2-Gy IR. Thirty fields, three repetitions. Magnification, 63×. (D) Costaining of H3K56ac (red) and γH2AX (green) in tissue niches 15 min after 6-Gy IR. Arrowheads indicate high H3K56ac levels and an abrogated γH2AX. Forty sections across four different mice. Magnification, 20×. DAPI = DNA. Scale bars, 10 μm. Representative images.

DSBs is unrelated to their radiosensitivity at or above clinical doses. In addition, most of these published studies did not compare stem cells with isogenic progeny or emphasize the use of early-passage, primary cultures. Prolonged passage of stem cells results in progressive epigenomic changes (Diaz Perez *et al.*, 2012), which we found can promote evolution of modified radioresponses (unpublished data). In agreement with our results, recent studies have found that both murine ES cells (Bañuelos *et al.*, 2008; Hennicke *et al.*, 2014) and induced pluripotent stem cells (Zhang *et al.*, 2013) exhibit deficient γH2AX induction and DNA repair. Although ES cells have been reported to exhibit high basal γH2AX levels even when untreated, this basal γH2AX is believed to be DDR independent (Banáth *et al.*, 2009) and could be an artifact of the unique chromatin environment in stem cells.

IRIF were observed in stem cells of the intestinal crypt (Hua *et al.*, 2012); however, that report did not address the fact that apoptosis was also observed in these same cells. Conversely, testicular stem cells were shown to exhibit abrogated γH2AX but without demonstrated IR-induced apoptosis (Rübe *et al.*, 2011). Radiation responses in brain have been studied only in a developmental context without specific stem cell markers (Gatz *et al.*, 2011), although evidence supports stem cell radiosensitivity within the SGZ (Peissner *et al.*, 1999; Mizumatsu *et al.*, 2003). Developmental heterogeneity inherent to stem cell populations may add to the complexity of radiation responses, as responses may potentially change throughout the cell cycle or as niches mature. Observed γH2AX at late time points either in vivo or in culture may also potentially be due to the onset of apoptotic pan-phosphorylation as opposed to DDR induction.

The previously studied relationship between γH2AX IRIF, pan-γH2AX, and H2AX-pY142 (Solier and Pommier, 2009) may explain how these modifications interact to contribute to stem cell radiosensitivity. Pan-γH2AX has been associated with both MDC1 inhibition (Solier and Pommier, 2011) and enhanced H2AX-Y142 phosphorylation through MST1 (Zhang *et al.*, 2012). We propose that the close proximity of persistent H2AX-pY142 sterically hinders access to the S139 site in stem cells, thereby inhibiting DDR signaling and promoting IR-induced apoptosis. Despite abrogated ATM-mediated γH2AX induction, the onset of apoptosis might induce chromatin changes that allow access to the break site to promote pan-γH2AX. This distinctive bimodal regulation of γH2AX underlies how epigenetic responses to DNA damage in stem cells act to bias toward a radiosensitive phenotype. Our discovery of persistent H2AX-pY142 suggests that whereas stem cells are able to sense DNA damage through the MRN complex and attempt to induce DDR signaling, γH2AX expansion and DDR amplification are impeded due to inhibited recruitment/retention of MDC1 (Soutoglou and Misteli, 2008).

We also showed that elevated H3K56ac in stem cells of the surveyed tissue types hinders DDR signaling and promotes radiosensitivity. This is in agreement with a recent report indicating that constitutive H3K56ac interferes with γH2AX and pATM induction (Zhu *et al.*, 2015). It is possible that H3K56ac in stem cells may even directly inhibit H2AX-pY142 dephosphorylation by blocking EYA recruitment. The literature has primarily assessed only global

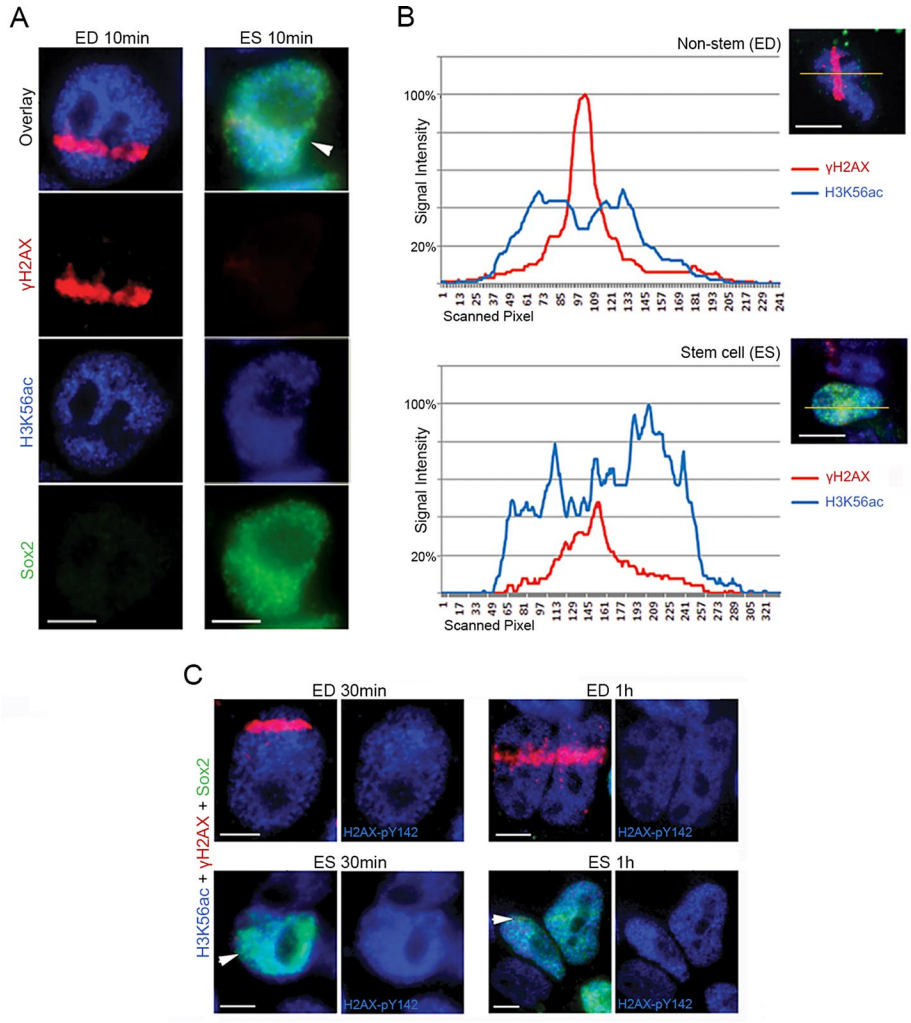

FIGURE 6: H3K56ac is transiently reduced at DSBs in non–stem cells. (A) Costaining of Sox2 (green), γH2AX (red), and H3K56ac (blue) on coplated ES and ED cells 10 min after microirradiation. $N = 50$. Arrowhead marks the microirradiation path. Magnification, 63×. (B) Signal intensity profiles of microirradiated ES and ED cells for H3K56ac (blue) and γH2AX (red) across the break site. Sox2, green. (C) Costaining of Sox2 (green), γH2AX (red) and H3K56ac (blue) on coplated ES and ED cells 30 min or 1 h after microirradiation. $N = 25$ for each time point. Arrowhead marks the microirradiation path. Magnification, 63×. Scale bars, 10 μm. Representative images. Microirradiation results were consistently observed in at least 75% of experiments.

changes in H3K56ac, with contradictory results concerning whether levels increase (Das *et al.*, 2009; Vempati *et al.*, 2010) or decrease (Tjeertes *et al.*, 2009; Miller *et al.*, 2010) after genotoxic stress. These inconsistencies may result from the dynamic nature of the H3K56ac radiation response, as we observed, which must be initially reduced and subsequently restored for efficient DDR processing (Battu *et al.*, 2011). Histone deacetylation at specific sites may be the mechanism responsible for the transient compaction of chromatin locally surrounding DSBs that has been found to be important for proper DDR signaling (Burgess *et al.*, 2014). Regulation of specific histone modifications may therefore determine the permissiveness of the surrounding chromatin environment for recruitment of repair factors to DSBs.

In addition to its role as an acetyltransferase, p300 acts as a transcriptional coactivator by directing assembly of transcriptional machinery at promoter regions (Kalkhoven, 2004). p300 promotes apoptosis (Yuan *et al.*, 1999) and positively regulates p53 in response to DNA damage (Avantaggiati *et al.*, 1997). It is therefore plausible that p300 knockdown could reduce radiosensitivity independent of H3K56ac. However, neither p53 (Aladjem *et al.*, 1998) nor its upstream kinase ATM (Lee *et al.*, 2001) is required for DNA damage–induced apoptosis in stem cells, and p53 would not influence the effects we observed on upstream DDR signaling. In addition, the I-CBP112 inhibitor only blocks interactions between the p300 bromodomain, acetylation targets, and the H3K56ac-specific histone chaperone ASF1 (Das *et al.*, 2014), leaving p300's transactivation function unhindered. Together with the lack of reduction in overall H3 or H4 acetylation levels after p300 knockdown, this suggests that the improved radiation responses observed in ES cells after p300 knockdown/inhibition are specific to H3K56ac down-regulation, substantiating its role as a potential therapeutic target.

Transient H3K56ac down-regulation only affected radiosensitivity and γH2AX induction in stem cells where H3K56ac levels are constitutively elevated, without any effect on differentiated cells. Because down-regulation was transient, long-term effects on stem cell pluripotency are not a concern. Our data suggest that there may be a threshold level of H3K56 acetylation during DDR signaling above which the recruitment of repair factors is inhibited, whereas further reduction below that threshold produces no additional benefit. H3K56ac might thus be serving as an epigenetic rheostat for modulating molecular radioresponses. Overall these data highlight the interconnections of epigenetic regulation, the DDR, and radiosensitivity.

The concerted effects of H2AX-pY142 and H3K56ac on DDR signaling and IR-induced apoptosis provide evidence of pluralistic epigenetic regulation of stem cell radiosensitivity. Although broad-acting epigenetic modifiers have been investigated for therapeutic value, focusing on specific histone modifications may prove more beneficial. These important findings thus provide strong conceptual advances in radiation oncology and stem cell biology, identifying potential new epigenetic targets for development of therapeutics to prevent stem cell depletion associated with radiotherapy and leading to added effectiveness of cancer treatment.

MATERIALS AND METHODS

Cell culture

Normal murine ES cells (EDJ22 or freshly isolated) were grown on gelatin-coated plates and passaged with 0.05% trypsin containing EDTA (Invitrogen, Grand Island, NY). They were differentiated by culturing in the absence of LIF (leukemia inhibitory factor) for several days. ES cells were used for only ~30 passages after initial acquisition to maintain early-passage phenotypes.

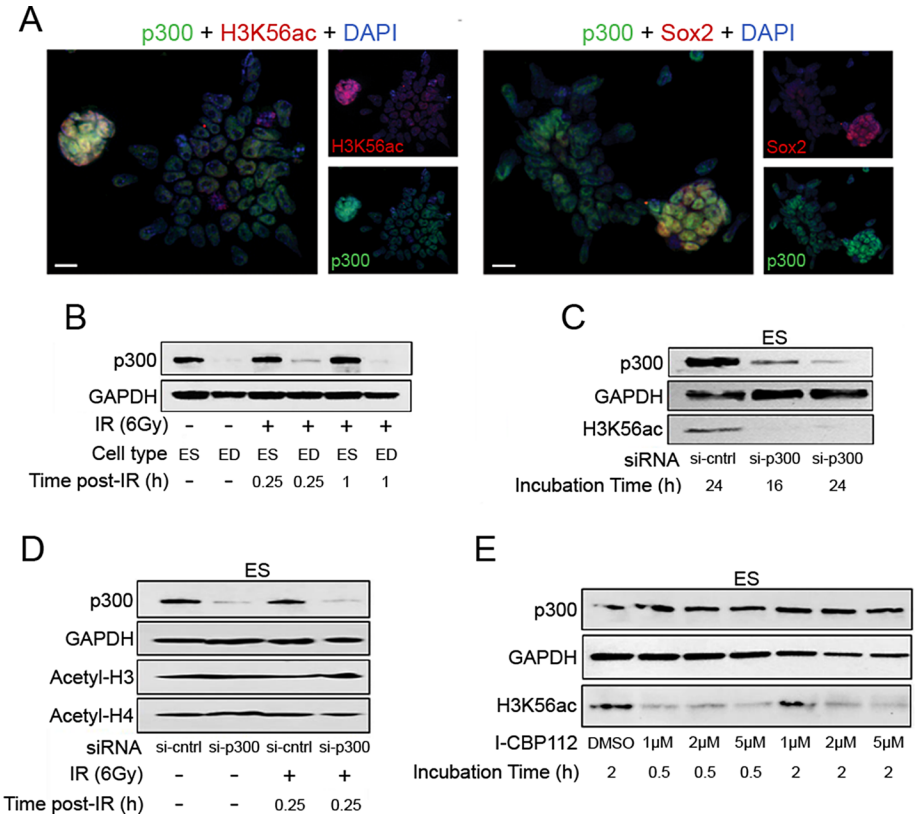

FIGURE 7: Elevated p300 acetyltransferase in stem cells regulates H3K56ac levels. (A) Costaining of p300 (green) and Sox2 (red, left) or H3K56ac (red, right) on an unirradiated differentiating ES cell colony. Ten colonies. Magnification, 20×. (B) Western blots for p300 at various time points after mock or 6-Gy irradiation of ES and ED cells. (C) Western blots for p300 and H3K56ac on ES cells after incubation for various times with p300-targeted or control siRNA. (D) Western blots for p300, acetyl-histone H3, and acetyl-histone H4 on ES cells incubated for 16 h with p300-targeted or control siRNA 15 min after sham or 6-Gy IR. (E) Western blots for p300 and H3K56ac on ES cells after incubation for various times with DMSO or I-CBP112 inhibitor. Scale bars, 10 μm. Representative images and blots.

Neural stem cells were freshly isolated from the hippocampus of brains from P0–P2 mouse pups and cultured in suspension after trituration. Neural stem cells were differentiated by addition of 10% fetal bovine serum (Hyclone, Logan, UT) and removal of EGF (epidermal growth factor)/FGF (fibroblast growth factor) from culture medium upon plating for attachment.

Animal models

Mouse strain C57BL/6 was used for all in vivo studies. Adult 6- to 8-wk-old males were used for tissue harvest/sectioning. P0xP2 mouse pups were killed by rapid decapitation before dissection for neural stem cell isolation. All animal procedures were approved by the Animal Studies Committee at Washington University Medical Center.

Antibodies

Supplemental Table S1 lists the antibodies used.

X-ray irradiation and tissue sectioning

Cells and animals were irradiated with 160-kV, 25-mA x-rays in the RS-2000 Biological Research Irradiator (Rad-Source, Suwanee, GA) at room temperature, with mock/control–irradiated samples brought into the room to simulate the reduction in ambient temperature and account for any stress imparted by the travel. Typical dose rate was 2–4 Gy/min. Cells were always placed within the central circle directly under the x-ray source to maintain consistency in dose between samples. Animals were anesthetized with isofluorane and placed on their back in the machine for whole-body irradiation to properly expose all tissues of interest to the x-ray source. Accuracy of all doses was confirmed by dosimeter probe. Both cells and animals were randomly assigned to individual time points or sham-irradiation controls. No statistical method was used to predetermine sample size for cellular or animal staining.

After irradiation, mice were killed at specific times by CO_2 asphyxiation and cervical dislocation. Organs were harvested, placed in OCT medium, and frozen in liquid nitrogen. Frozen tissues were sectioned on a cryostat machine at a thickness of 10 μm, placed onto adhesion slides, and stored at –80°C.

Apoptosis assays

Apoptosis in cultured cells was analyzed by flow cytometry using terminal deoxynucleotidyl transferase dUTP nick end labeling (TUNEL) and annexin V assays following manufacturer's protocol. An APO-BrdU TUNEL Assay Kit with Alexa Fluor 488 Anti-BrdU (Invitrogen) was used for the TUNEL assay, and an annexin V fluorescein isothiocyanate detection kit (BD Biosciences, San Jose, CA) was used for annexin V staining. Altogether 10,000 gated cells were counted for flow cytometry analysis. TUNEL staining on tissue sections was performed with the DeadEND fluorescent TUNEL system (Promega, Madison, WI).

Western blotting

Cellular protein lysates were collected in RIPA buffer, electrophoresed on 4–15% Tris-glycine polyacrylamide gels (Bio-Rad, Hercules, CA), transferred onto polyvinylidene fluoride membranes, and incubated overnight at 4°C with various primary antibodies, followed by washing and secondary antibody incubation for 2 h at room temperature. Super ECL (GE, Pittsburgh, PA) was used as substrate for detection on autoradiography film or a ChemiDoc MP digital system (Bio-Rad). All Western blots shown in this study are representative images of successful experiments repeated at least twice on unique samples of cellular lysate.

Immunofluorescence

Freshly frozen tissues were isolated from the testis, brain, intestine, and skin after 6-Gy irradiation or 0-Gy mock before embedding in OCT medium and sectioning onto slides. Slides of tissue sections or coverslips of cells were fixed in 4% formaldehyde and permeabilized with 0.2% Triton-X, followed by blocking with 2% bovine serum albumin (BSA). Tissues were incubated with primary antibodies in 1% BSA at 37°C for 3 h, washed, and then incubated with secondary fluorescently tagged secondary antibodies for 45 min at 37°C. Tissues were then mounted in place with coverslips containing mounting medium with 4′,6-diamidino-2-phenylindole (DAPI; Vector, Burlingame, CA) for identification of nuclei. Tissue staining

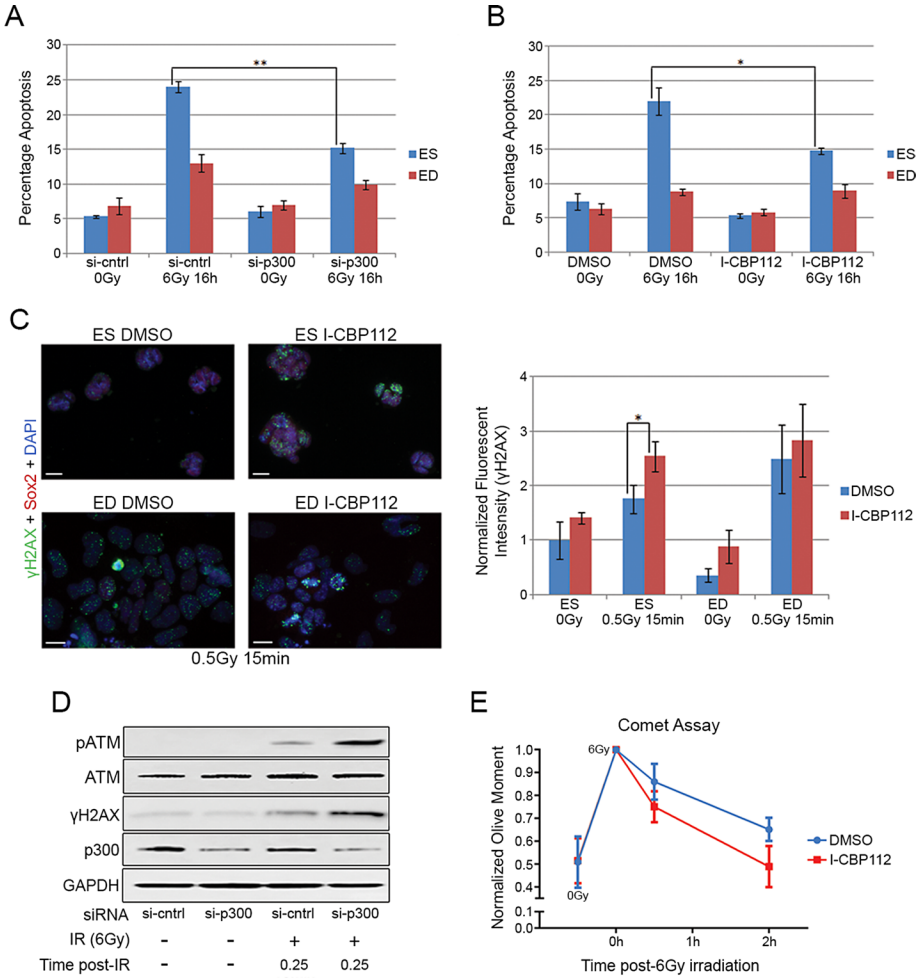

FIGURE 8: H3K56ac reduction improves radiation responses of stem cells. (A, B) Flow cytometric analysis of apoptosis comparing ES and ED cells by annexin V labeling 12 h after either sham or 6-Gy IR after (A) incubation for 16 h (ES) or 24 h (ED) with p300-targeted or control siRNA and (B) incubation for 1 h with DMSO or 5 μM I-CBP112 inhibitor. We counted 10,000 gated cells. $N = 3$; *$p < 0.05$, **$p < 0.01$, otherwise not significant. (C) Costaining of γH2AX (green) and Sox2 (red) on ES and ED cells 15 min after sham or 0.5-Gy IR after incubation for 1 h with DMSO or 5μM I-CBP112 inhibitor. Left, 0.5-Gy IR; right, quantification of γH2AX fluorescence intensity per cell normalized to ES 0-Gy sample. From 20 to120 cells were scored per field. $N = 10$ fields/sample; *$p < 0.05$; otherwise not significant. Magnification, 20×. (D) Western blots for p300, pATM (S1981), ATM, and γH2AX on ES cells incubated for 16 h with p300-targeted or control siRNA after sham or 6-Gy IR. GAPDH was loading control. (E) Olive moments of comet assay tails from ES cells at different time points after sham or 6-Gy IR normalized to the irradiated 0-min time point after incubation for 1 h with DMSO or 5 μM I-CBP112 inhibitor; 50–75 comets scored per sample. $N = 4$. ANCOVA for the entire curve, $p = 0.046$. Error bars indicate SEM. DAPI = DNA. Scale bars, 10 μm. Representative images.

for all experiments was successfully repeated on at least three sections from three independent tissue isolations of different mice.

Cells were similarly fixed in 4% formaldehyde and permeabilized with 0.2% Triton-X before blocking. For double-color staining, primary antibodies were incubated together for 1 h at 37°C, followed by wash and incubation with fluorescently tagged secondary antibodies for 30 min at 37°C. For triple-color staining, before mounting, cells were incubated with 1:1000 α-γH2AX antibody for 15 min at 37°C, followed by a 12-min incubation at 37°C with the appropriate secondary antibody. Anti-γH2AX antibody was chosen to match Sox2 to avoid cross-reaction with the other target antigens of interest. Immunofluorescence data from all figures show representative images of experiments with the biological phenomenon successfully observed at least three times.

Neutral comet assay

To assess repair of DNA double-strand breaks, neutral comet assays were performed using CometSlide assay kits (Trevigen). Cells were collected at multiple times after 6-Gy irradiation or 0-Gy mock and embedded in agarose on slides at equal concentrations. Slides were electrophoresed in TAE (Tris acetate EDTA) buffer, fluorescently stained with SYBR Green (Trevigen, Gaithersburg, MD), and visualized by fluorescence microscopy. The olive comet moment was calculated using CometScore software (TriTek, Sumerduck, VA) to analyze 50–100 comets/sample, with each series of time points repeated at least three independent times as both biological and technical replicates. Individual comets were randomly selected for scoring from similar regions of the slide in all samples. Outliers were eliminated that fell >1.5 SDs from the mean. Standard error was calculated for each cell type and time point normalized to the value of the 0-min samples, and the significance of the difference between cell types over time was analyzed by analysis of covariance (ANCOVA) using XLStat statistical software (Addinsoft, New York, NY), with two-sided significance set at $p < 0.05$. ANCOVA measures the divergence of the slopes of two curves, therefore assessing the significance of DNA repair differences throughout the entire time course as opposed to at a single time point. Data from all samples were approximately normally distributed, and the SD between samples within the same experiment was similar. Samples were excluded from analysis only due to technical errors from the assay or cells being visibly unhealthy.

Clonogenic survival assay

Cells were used in a colony formation assay to measure cell survival after IR treatment using standard protocols. Cells were plated, irradiated 6 h later at various doses, and allowed to grow for 7–14 d. Any colonies formed were fixed and stained with crystal violet (Sigma-Aldrich, St. Louis, MO). The number of colonies (with >50 cells) per dish was counted, and the surviving fractions were calculated as the ratio of the plating efficiencies of treated cells to untreated cells.

Bromodeoxyuridine pulse-chase

ES and ED cells were incubated with 20 μM bromodeoxyuridine (BrdU; Sigma-Aldrich) for 30 min, washed twice, and chased for the appropriate time. Cells were then fixed overnight in ethanol, washed, incubated with 100 μg/ml RNase (Thermo Scientific, Waltham, MA) for 30 min at 37°C, and labeled with propidium iodide (BD Biosciences). Cell cycle progression was then visualized by flow cytometry.

Factor	Status after DNA damage in stem cells	Status after DNA damage in non–stem cells
DDR sensors		
Nbs1	Present	Present
Ku80	Present	Present
DDR transducers		
pATM	Attenuated	Activated/recruited
pATR	Attenuated	Activated
DDR mediators		
γH2AX	Attenuated	Induced
MDC1	Attenuated	Recruited
DDR effector		
pChk1	Attenuated	Activated
DNA repair factors		
pDNA-PK	Attenuated	Activated/recruited
Rad51	Attenuated	Recruited
Apoptotic signaling		
Bax	Enhanced	Reduced
Bcl-2	Reduced	Enhanced
Cleaved PARP	Induced	Absent
Cleaved caspase-3	Induced	Absent
pMST1	Activated/recruited	Absent
pJNK	Activated/recruited	Absent
Pan-γH2AX	Induced	Absent
Epigenetic regulators of DDR		
H2AX-pY142	Present after damage	Absent after damage
H3K56ac	High, no change at DSBs	Low, transiently reduced at DSBs
p300	High, reduction improves radiation responses through H3K56ac down-regulation	Low, reduction has no statistically significant effect on radiation responses despite H3K56ac down-regulation

TABLE 1: Summary of the DDR and IR-induced apoptosis in stem cells and non–stem cells.

p300 knockdown and inhibition

Mouse nonspecific control or p300-targeted SMARTpool siRNA (Dharmacon, Lafayette, CO) was transfected at a concentration of 20 nM using Lipofectamine RNAiMAX transfection reagent (Invitrogen) following the manufacturer's recommendations for transient knockdown. siRNA sequences are provided in Supplemental Table S2. SMARTpool siRNA uses a series of oligomers together to improve targeting efficiency and specificity. Incubation time was optimized to allow for protein degradation after genetic knockdown. Maximum knockdown of p300 and H3K56ac occurred after 16 h of incubation in ES cells and 24 h in ED cells. Nonspecific siRNA served as a negative vehicle control for comparison in parallel with p300-knockdown samples. For pharmacological inhibition of p300, incubation with I-CBP112 (Cayman Chemical, Ann Arbor, MI) was optimized as 5 μM for 1 h. Cells were washed with phosphate-buffered saline to remove I-CBP112 30 min after irradiation to ensure only a transient reduction of H3K56ac. Cells were incubated with dimethyl sulfoxide (DMSO) as a negative vehicle control in parallel for comparison.

γH2AX foci quantification

ES and ED cells were coplated on coverslips and incubated with either DMSO or 5 μM I-CBP112 for 1 h. Samples were then exposed to either mock or 0.5-Gy IR and incubated for 15 min before fixation and immunofluorescence staining. Consistent settings were used to obtain images for comparison through each color channel by fluorescence microscopy. Integrated density was measured using ImageJ (National Institutes of Health, Bethesda, MD) for γH2AX in each field after elimination of background using region-of-interest polygon selections and thresholding >15 U. Total integrated density of each field was then divided by the number of cells to obtain the average fluorescence intensity per cell, and values were normalized relative to the ES 0-Gy sample.

Subnuclear microirradiation

Stem cells (ES, NS) were coplated with non–stem cells (ED, mouse embryonic fibroblast) on glass coverslips and incubated for 2 d with 30 μM BrdU (Sigma-Aldrich) to sensitize DNA for DSB induction. Before laser microirradiation, cells were incubated with Stem Cell cDy1 Dye (Active Motif, Carlsbad, CA) for 30 min to fluorescently label live stem cells for identification. Coverslips were then placed in circular magnetic chambers (Quorum Technologies, Guelph, Canada) with media to be properly aligned for microirradiation. Cells were microirradiated in a defined narrow region across adjacent stem cells and non–stem cells with 8000–12,000 iterations of

405- and 633-nm lasers on an LSM 510 Confocal Microscope (Zeiss, Oberkochen, Germany) at 45% power output. Care was taken to include stem cells (cDy1 positive) as well as non–stem cells in the DNA damage tracks. Cells were microirradiated for 20–30 min/sample unless otherwise stated, with 6–12 regions of microirradiation per sample. Fluorescence signal intensity profiles were quantified across the nucleus through the microirradiation track using MetaSystems ISIS imaging and analysis software. Microirradiation and subsequent immunofluorescence staining were repeated for specific samples and target proteins a minimum of 5–10 times/sample.

Cytogenetic analysis

Cells were incubated with 100 ng/ml Colcemid for 2–4 h after either mock or 2–4 Gy irradiation to arrest cells in metaphase. Mitotic cells were selectively isolated by mitotic shake-off, incubated in hypotonic buffer (0.56% KCl) for 8 min, fixed in acetate-methanol, and dropped onto slides. Fluorescence in situ hybridization was performed using oligonucleotide $(TTAGGG)_3$ PNA probes using standard protocols and counterstained with DAPI. Chromosomes were then visualized by fluorescence microscopy and scored for chromosome aberrations. The number of chromosome aberrations was normally distributed for each sample, with similar SDs between samples from the same time point. Each sample was repeated three times. Chromosome aberrations were defined as chromosome or chromatid breaks, translocations, or radials. Standard error was calculated, and statistical significance was determined by Student's *t* test, with two-sided significance set at $p < 0.05$. Only full chromosome plates were scored; any partial plates were excluded from scoring.

Microscopy and image processing

Micrographs were captured using MetaSystems ISIS imaging and analysis software on a Zeiss Axioplan 2 microscope or ZEN software on a Zeiss LSM510 confocal microscope with 20×, 63×, and 100× objective lenses. Minimal threshold and contrast manipulation was performed equally across entire images. Controls were processed equally with treated samples. Adobe Photoshop CS3 software was used for minor processing of images. All processing was performed equally on the entire image.

Statistical analysis

A two-tailed unpaired Student's t test was used to calculate the statistical significance of the observed differences. ANCOVA was used to determine the significance of differences in comet assay curves across an entire time course. In all cases, differences were considered statistically significant when $p < 0.05$. Unless otherwise indicated, graphed values represent mean ± SEM.

ACKNOWLEDGMENTS

We thank Steven Mennerick and Ann Benz for demonstrating mouse hippocampal microdissection. This work is supported by the National Institutes of Health (R01CA174966) and the Department of Radiation Oncology and Siteman Cancer Center, Washington University School of Medicine.

REFERENCES

Acharya MM, Lan ML, Kan VH, Patel NH, Giedzinski E, Tseng BP, Limoli CL (2010). Consequences of ionizing radiation-induced damage in human neural stem cells. Free Radic Biol Med 49, 1846–1855.

Adams BR, Hawkins AJ, Povirk LF, Valerie K (2010). ATM-independent, high-fidelity nonhomologous end joining predominates in human embryonic stem cells. Aging (Albany NY) 2, 582–596.

Aladjem MI, Spike BT, Rodewald LW, Hope TJ, Klemm M, Jaenisch R, Wahl GM (1998). ES cells do not activate p53-dependent stress responses and undergo p53-independent apoptosis in response to DNA damage. Curr Biol 8, 145–155.

Ash P (1980). The influence of radiation on fertility in man. Br J Radiol 53, 271–278.

Avantaggiati ML, Ogryzko V, Gardner K, Giordano A, Levine AS, Kelly K (1997). Recruitment of p300/CBP in p53-dependent signal pathways. Cell 89, 1175–1184.

Banáth JP, Bañuelos CA, Klokov D, MacPhail SM, Lansdorp PM, Olive PL (2009). Explanation for excessive DNA single-strand breaks and endogenous repair foci in pluripotent mouse embryonic stem cells. Exp Cell Res 315, 1505–1520.

Bañuelos CA, Banáth JP, MacPhail SH, Zhao J, Eaves CA, O'Connor MD, Lansdorp PM, Olive PL (2008). Mouse but not human embryonic stem cells are deficient in rejoining of ionizing radiation-induced DNA double-strand breaks. DNA Repair (Amst) 7, 1471–1483.

Battu A, Ray A, Wani AA (2011). ASF1A and ATM regulate H3K56-mediated cell-cycle checkpoint recovery in response to UV irradiation. Nucleic Acids Res 39, 7931–7945.

Burgess RC, Burman B, Kruhlak MJ, Misteli T (2014). Activation of DNA damage response signaling by condensed chromatin. Cell Rep 9, 1703–1717.

Burma S, Chen BP, Murphy M, Kurimasa A, Chen DJ (2001). ATM phosphorylates histone H2AX in response to DNA double-strand breaks. J Biol Chem 276, 42462–42467.

Celeste A, Fernandez-Capetillo O, Kruhlak MJ, Pilch DR, Staudt DW, Lee A, Bonner RF, Bonner WM, Nussenzweig A (2003). Histone H2AX phosphorylation is dispensable for the initial recognition of DNA breaks. Nat Cell Biol 5, 675–679.

Chuykin IA, Lianguzova MS, Pospelova TV, Pospelov VA (2008). Activation of DNA damage response signaling in mouse embryonic stem cells. Cell Cycle 7, 2922–2928.

Cook PJ, Ju BG, Telese F, Wang X, Glass CK, Rosenfeld MG (2009). Tyrosine dephosphorylation of H2AX modulates apoptosis and survival decisions. Nature 458, 591–596.

Das C, Lucia MS, Hansen KC, Tyler JK (2009). CBP/p300-mediated acetylation of histone H3 on lysine 56. Nature 459, 113–117.

Das C, Roy S, Namjoshi S, Malarkey CS, Jones DNM, Kutateladze TG, Churchill MEA, Tyler JK (2014). Binding of the histone chaperone ASF1 to the CBP bromodomain promotes histone acetylation. Proc Natl Acad Sci USA 111, E1072–E1081.

Del Re DP, Matsuda T, Zhai P, Maejima Y, Jain MR, Liu T, Li H, Hsu C-P, Sadoshima J (2014). Mst1 promotes cardiac myocyte apoptosis through phosphorylation and inhibition of Bcl-xL. Mol Cell 54, 639–650.

Diaz Perez SV, Kim R, Li Z, Marquez VE, Patel S, Plath K, Clark AT (2012). Derivation of new human embryonic stem cell lines reveals rapid epigenetic progression in vitro that can be prevented by chemical modification of chromatin. Hum Mol Genet 21, 751–764.

Duffner PK (2004). Long-term effects of radiation therapy on cognitive and endocrine function in children with leukemia and brain tumors. Neurologist 10, 293–310.

Fox N, Damjanov I, Knowles BB, Solter D (1983). Immunohistochemical localization of the mouse stage-specific embryonic antigen 1 in human tissues and tumors. Cancer Res 43, 669–678.

Gatz SA, Ju L, Gruber R, Hoffmann E, Carr AM, Wang Z-Q, Liu C, Jeggo PA (2011). Requirement for DNA ligase IV during embryonic neuronal development. J Neurosci 31, 10088–10100.

Greenberger JS ((2009). Radioprotection. In Vivo 23, 323–336.

Hellman S, Botnick LE (1977). Stem cell depletion: an explanation of the late effects of cytotoxins. Int J Radiat Oncol Biol Phys 2, 181–184.

Hennicke T, Nieweg K, Brockmann N, Kassak MU, Gottman K, Fritz G (2014). mESC-based in vitro differentiation models to study vascular response and functionality following genotoxic insults. Toxicol Sci 144, 138–150.

Hua G, Thin TH, Feldman R, Haimovitz-Friedman A, Clevers H, Fuks Z, Kolesnick R (2012). Crypt base columnar stem cells in small intestines of mice are radioresistant. Gastroenterology 143, 1266–1276.

Jackson SP, Bartek J (2009). The DNA-damage response in human biology and disease. Nature 461, 1071–1078.

Kalkhoven E (2004). CBP and p300: HATs for different occasions. Biochem Pharmacol 68, 1145–1155.

Koike M, Koike A (2008). Accumulation of Ku80 proteins at DNA double-strand breaks in living cells. Exp Cell Res 314, 1061–1070.

Lee J-H, Paull TT (2007). Activation and regulation of ATM kinase activity in response to DNA double-strand breaks. Oncogene 26, 7741–7748.

Lee Y, Chong MJ, McKinnon PJ (2001). Ataxia telangiectasia mutated-dependent apoptosis after genotoxic stress in the developing nervous system is determined by cellular differentiation status. J Neurosci 21, 6687–6693.

Liu JC, Guan X, Ryan JA, Rivera AG, Mock C, Agarwal V, Letai A, Lerou PH, Lahav G (2013). High mitochondrial priming sensitizes hESCs to DNA-damage-induced apoptosis. Cell Stem Cell 13, 483–491.
Lu C, Zhu F, Cho Y-Y, Tang F, Zykova T, Ma W, Bode AM, Dong Z (2006). Cell apoptosis: requirement of H2AX in DNA ladder formation, but not for the activation of caspase-3. Mol. Cell 23, 121–132.
Lukas J, Lukas C, Bartek J (2011). More than just a focus: the chromatin response to DNA damage and its role in genome integrity maintenance. Nat Cell Biol 13, 1161–1169.
Martin DD (2011). Review of radiation therapy in the pregnant cancer patient. Clin Obstet Gynecol 54, 591–601.
Miller KM, Tjeertes JV, Coates J, Legube G, Polo SE, Britton S, Jackson SP (2010). Human HDAC1 and HDAC2 function in the DNA-damage response to promote DNA nonhomologous end-joining. Nat Struct Mol Biol 17, 1144–1151.
Mizumatsu S, Monje ML, Morhardt DR, Rola R, Palmer TD, Fike JR (2003). Extreme sensitivity of adult neurogenesis to low doses of X-irradiation. Cancer Res 63, 4021–4027.
Norbury CJ, Zhivotovsky B (2004). DNA damage-induced apoptosis. Oncogene 23, 2797–2808.
Paull TT, Rogakou EP, Yamazaki V, Kirchgessner CU, Gellert M, Bonner WM (2000). A critical role for histone H2AX in recruitment of repair factors to nuclear foci after DNA damage. Curr Biol 10, 886–895.
Peissner W, Kocher M, Treuer H, Gillardon F (1999). Ionizing radiation-induced apoptosis of proliferating stem cells in the dentate gyrus of the adult rat hippocampus. Brain Res Mol Brain Res 71, 61–68.
Pesce M, Wang X, Wolgemuth DJ, Schöler H (1998). Differential expression of the Oct-4 transcription factor during mouse germ cell differentiation. Mech Dev 71, 89–98.
Praskova M, Khoklatchev A, Ortiz-Vega S, Avruch J (2004). Regulation of the MST1 kinase by autophosphorylation, by the growth inhibitory proteins, RASSF1 and NORE1, and by Ras. Biochem J 381, 453–462.
Rübe CE, Zhang S, Miebach N, Fricke A, Rübe C (2011). Protecting the heritable genome: DNA damage response mechanisms in spermatogonial stem cells. DNA Repair (Amst) 10, 159–168.
Schneider L, Fumagalli M, d'Adda di Fagagna F (2011). Terminally differentiated astrocytes lack DNA damage response signaling and are radioresistant but retain DNA repair proficiency. Cell Death Differ 19, 582–591.
Smith DH, DeCosse JJ (1986). Radiation damage to the small intestine. World J Surg 10, 189–194.
Solier S, Pommier Y (2009). The apoptotic ring: a novel entity with phosphorylated histones H2AX and H2B and activated DNA damage response kinases. Cell Cycle 8, 1853–1859.
Solier S, Pommier Y (2011). MDC1 cleavage by caspase-3: a novel mechanism for inactivating the DNA damage response during apoptosis. Cancer Res 71, 906–913.
Sotiropoulou PA, Candi A, Mascre G, De Clercq S, Youssef KK, Lapouge G, Dahl E, Semeraro C, Denecker G, Marine JC, *et al.* (2010). Bcl-2 and accelerated DNA repair mediates resistance of hair follicle bulge stem cells to DNA-damage-induced cell death. Nat Cell Biol 12, 572–582.
Soutoglou E, Misteli T (2008). Activation of the cellular DNA damage response in the absence of DNA lesions. Science 320, 1507–1510.
Sugrue T, Brown JAL, Lowndes NF, Ceredig R (2013). Multiple facets of the DNA damage response contribute to the radioresistance of mouse mesenchymal stromal cell lines. Stem Cells 31, 137–145.
Suh H, Consiglio A, Ray J, Sawai T, D'Amour KA, Gage FH (2007). In vivo fate analysis reveals the multipotent and self-renewal capacities of Sox2+ neural stem cells in the adult hippocampus. Cell Stem Cell 1, 515–528.
Tichy ED, Pillai R, Deng L, Liang L, Tischfield J, Schwemberger SJ, Babcock GF, Stambrook PJ (2010). Mouse embryonic stem cells, but not somatic cells, predominantly use homologous recombination to repair double-strand DNA breaks. Stem Cells Dev 19, 1699–1711.
Tjeertes JV, Miller KM, Jackson SP (2009). Screen for DNA-damage-responsive histone modifications identifies H3K9Ac and H3K56Ac in human cells. EMBO J 28, 1878–1889.
Ura S, Nishina H, Gotoh Y, Katada T (2007). Activation of the c-Jun N-terminal kinase pathway by MST1 is essential and sufficient for the induction of chromatin condensation during apoptosis. Mol Cell Biol 27, 5514–5522.
Vempati RK, Jayani RS, Notani D, Sengupta A, Galande S, Haldar D (2010). p300-mediated acetylation of histone H3 lysine 56 functions in DNA damage response in mammals. J Biol Chem 285, 28553–28564.
Wen W, Zhu F, Zhang J, Keum YS, Zykova T, Yao K, Peng C, Zheng D, Cho YY, Ma WY, *et al.* (2010). MST1 promotes apoptosis through phosphorylation of histone H2AX. J Biol Chem 285, 39108–39116.
Xiao A, Li H, Shechter D, Ahn SH, Fabrizio LA, Erdjument-Bromage H, Ishibe-Murakami S, Wang B, Tempst P, Hofmann K, *et al.* (2009). WSTF regulates the H2A.X DNA damage response via a novel tyrosine kinase activity. Nature 457, 57–62.
Xie W, Song C, Young NL, Sperling AS, Xu F, Sridharan R, Conway AE, Garcia BA, Plath K, Clark AT, *et al.* (2009). Histone h3 lysine 56 acetylation is linked to the core transcriptional network in human embryonic stem cells. Mol Cell 33, 417–427.
Yuan J, Chen J (2010). MRE11-RAD50-NBS1 complex dictates DNA repair independent of H2AX. J Biol Chem 285, 1097–1104.
Yuan ZM, Huang Y, Ishiko T, Nakada S, Utsugisawa T, Shioya H, Utsugisawa Y, Shi Y, Weichselbaum R, Kufe D (1999). Function for p300 and not CBP in the apoptotic response to DNA damage. Oncogene 18, 5714–5717.
Zhang M, Yang C, Liu H, Sun Y (2013). Induced pluripotent stem cells are sensitive to DNA damage. Genomics Proteomics Bioinformatics 11, 320–326.
Zhang Y, Lu C, Cao Y, Luo Y, Bao R, Yan S, Xue M, Zhu F, Wang Z, Duan L (2012). Imatinib induces H2AX phosphorylation and apoptosis in chronic myelogenous leukemia cells in vitro via caspase-3/Mst1 pathway. Acta Pharmacol Sin 33, 551–557.
Zhu Q, Battu A, Ray A, Wani G, Qian J, He J, Wang Q-E, Wani AA (2015). Damaged DNA-binding protein down-regulates epigenetic mark H3K56Ac through histone deacetylase 1 and 2. Mutat Res 776, 16–23.
Zou Y, Zhang N, Ellerby LM, Davalos AR, Zeng X, Campisi J, Desprez P-Y (2012). Responses of human embryonic stem cells and their differentiated progeny to ionizing radiation. Biochem Biophys Res Commun 426, 100–105.

Supplemental Materials

Molecular Biology of the Cell

Jacobs et al.

SUPPLEMENTARY FIGURE S1

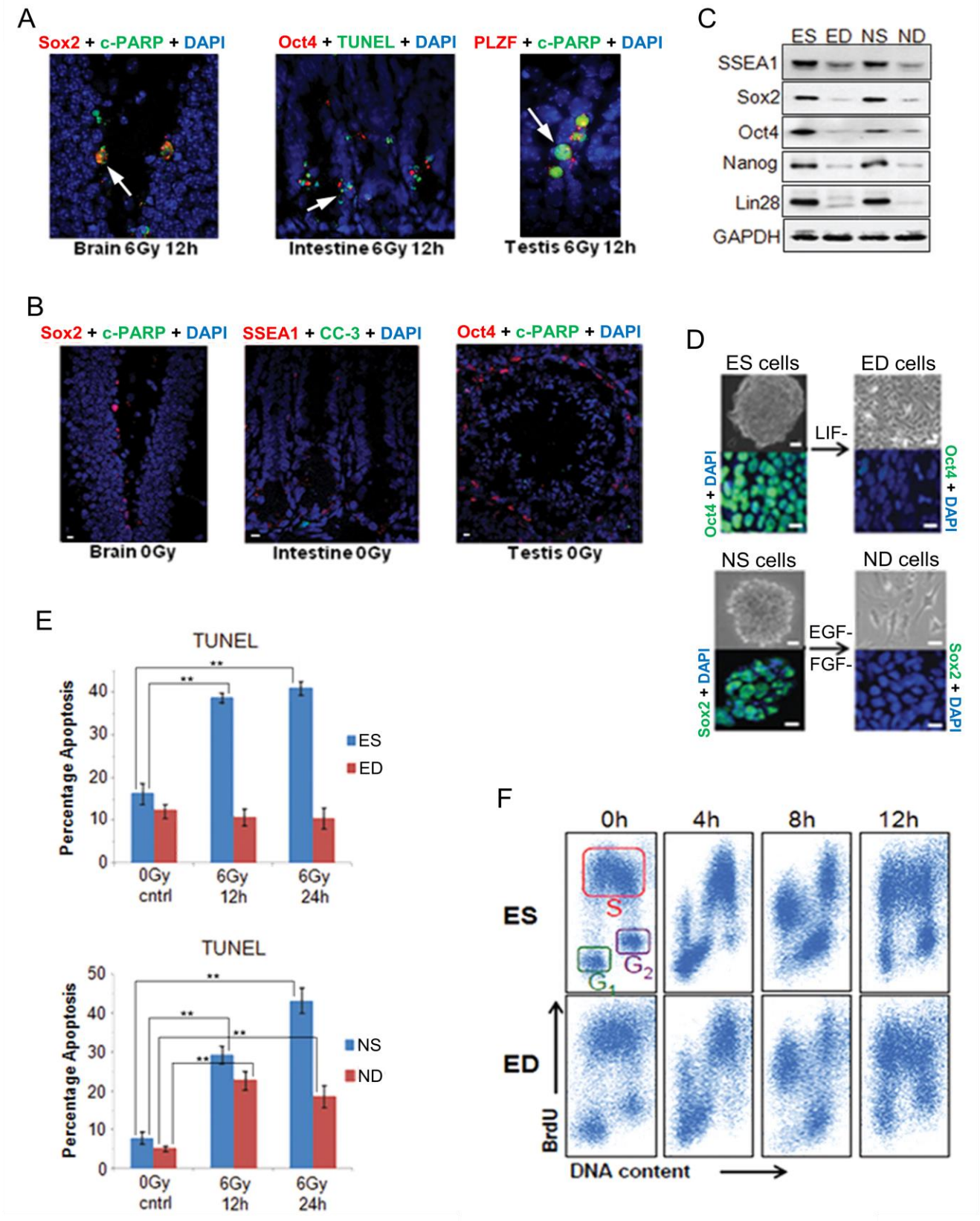

Supplementary Figure S1, related to Figure 1.

(A) Co-staining of Sox2 (red) and cleaved PARP (c-PARP, green) in brain, Oct4 (red) and TUNEL stain (green) in intestine, and Oct4 (red) and c-PARP (green) in testis 12h following 6Gy irradiation. Punctate staining is due to nuclear fragmentation upon apoptosis. Arrows indicate stem cells undergoing apoptosis. N=25 sections across 5 different mice. Magnification, 63x. (B) Co-staining of Sox2 (red) and cleaved PARP (c-PARP, green) in brain, SSEA1 (red) and cleaved Caspase-3 (CC-3, green) in intestine, and Oct4 (red) and c-PARP (green) in testis following sham irradiation. N=25 sections across 5 different mice. Magnification, 20x. (C) Western blots for stem cell markers on unirradiated ES, ED, NS and ND cells. GAPDH is loading control. (D) Bright field images and immunofluorescence staining for stem cell markers (green) demonstrating differentiation of ES cells into ED cells and NS cells into ND cells. N=100 colonies/neurospheres. Magnification, 20x (bright field), 63x (fluorescent). (E) Flow cytometric analysis of apoptosis comparing ES and ED or NS and ND cells by TUNEL labeling following sham or 6Gy IR at indicated timepoints. 10,000 gated cells were counted, N=3; ** = $p < 0.01$; otherwise not significant. Error bars indicate SEM. (F) BrdU pulse-chase profiles measuring cell cycle length of unirradiated ES and ED cells. Rectangles indicate the presence of G1, S, and G2 populations. 20,000 gated cells were counted for analysis. DAPI=DNA. White scale bars, 10μm. Representative images and blots are shown.

SUPPLEMENTARY FIGURE S2

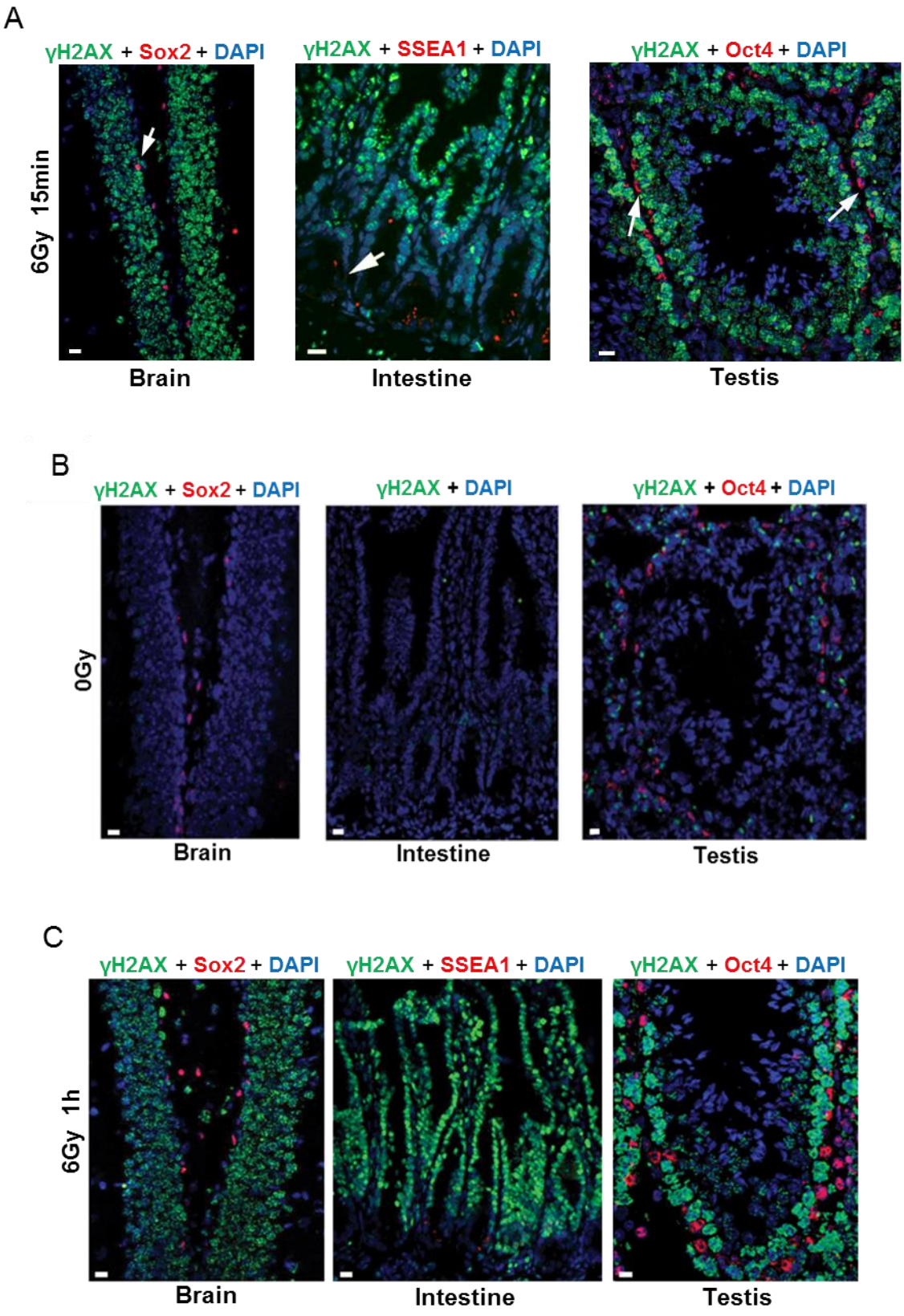

Supplementary Figure S2, related to Figure 2.

(A) Co-staining of γH2AX (green) and stem cell marker (red) Sox2 in brain, SSEA1 in intestine, and Oct4 in testis 15min following 6Gy IR. Arrows indicate stem cells lacking γH2AX. Magnification, 20x (brain), 25x (intestine), 63x (testis). (B) Co-staining of γH2AX (green) and stem cell marker (red) Sox2 in brain , SSEA1 in intestine, and Oct4 in testis following sham irradiation. N=20 sections (each tissue) across 4 different mice. Magnification, 20x. (C) Co-staining of stem cell markers (red) and γH2AX (green) in tissue niches 1h following 6Gy IR. N=20 sections (each tissue) across 4 different mice Magnification, 20x. DAPI=DNA. White scale bars, 10μm. Representative images are shown.

SUPPLEMENTARY FIGURE S3

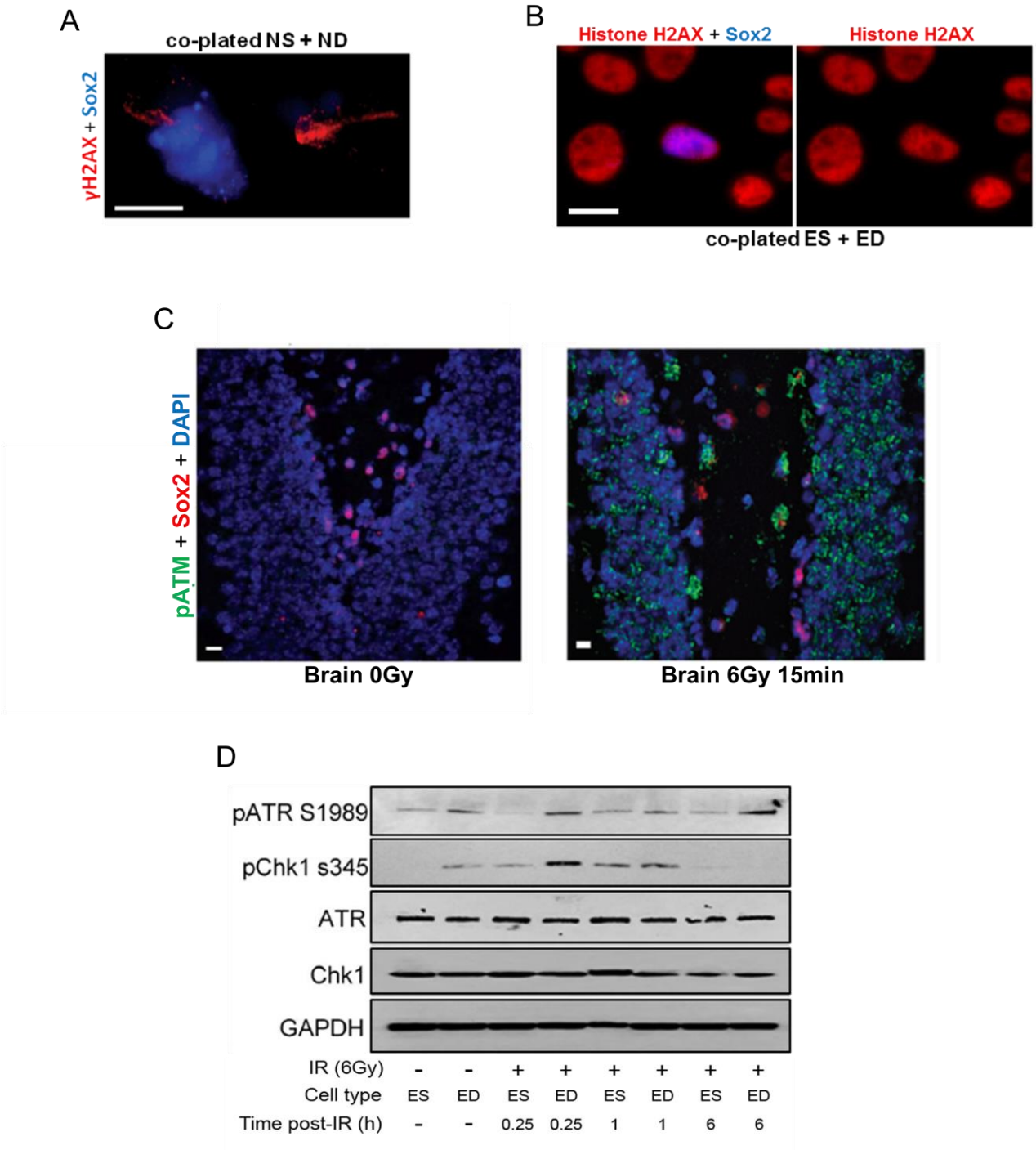

Supplementary Figure S3, related to Figure 2.

(A) Co-staining of Sox2 (blue) and γH2AX (S139, red) on co-plated NS and ND cells following microirradiation, N=40. Magnification, 63x. (B) Co-staining of Sox2 (blue) and histone H2AX (red) on co-plated unirradiated ES and ED cells. N=20 fields, 3 repetitions. Magnification, 63x. (C) Co-staining of Sox2 (red) and pATM (S1981, green) in brain 15min following sham or 6Gy irradiation. N=20 sections (each tissue) across 4 different mice. Magnification, 20x. (D) Western blots for pATR (S1989), total ATR, pChk1 (S345) and total Chk1 on ES and ED cells at various time points following mock or 6Gy irradiation of ES and ED cells. GAPDH is loading control. DAPI=DNA. White scale bars, 10μm. Representative images and blots shown. Microirradiation results were consistently observed in at least 75% of experiments.

SUPPLEMENTARY FIGURE S4

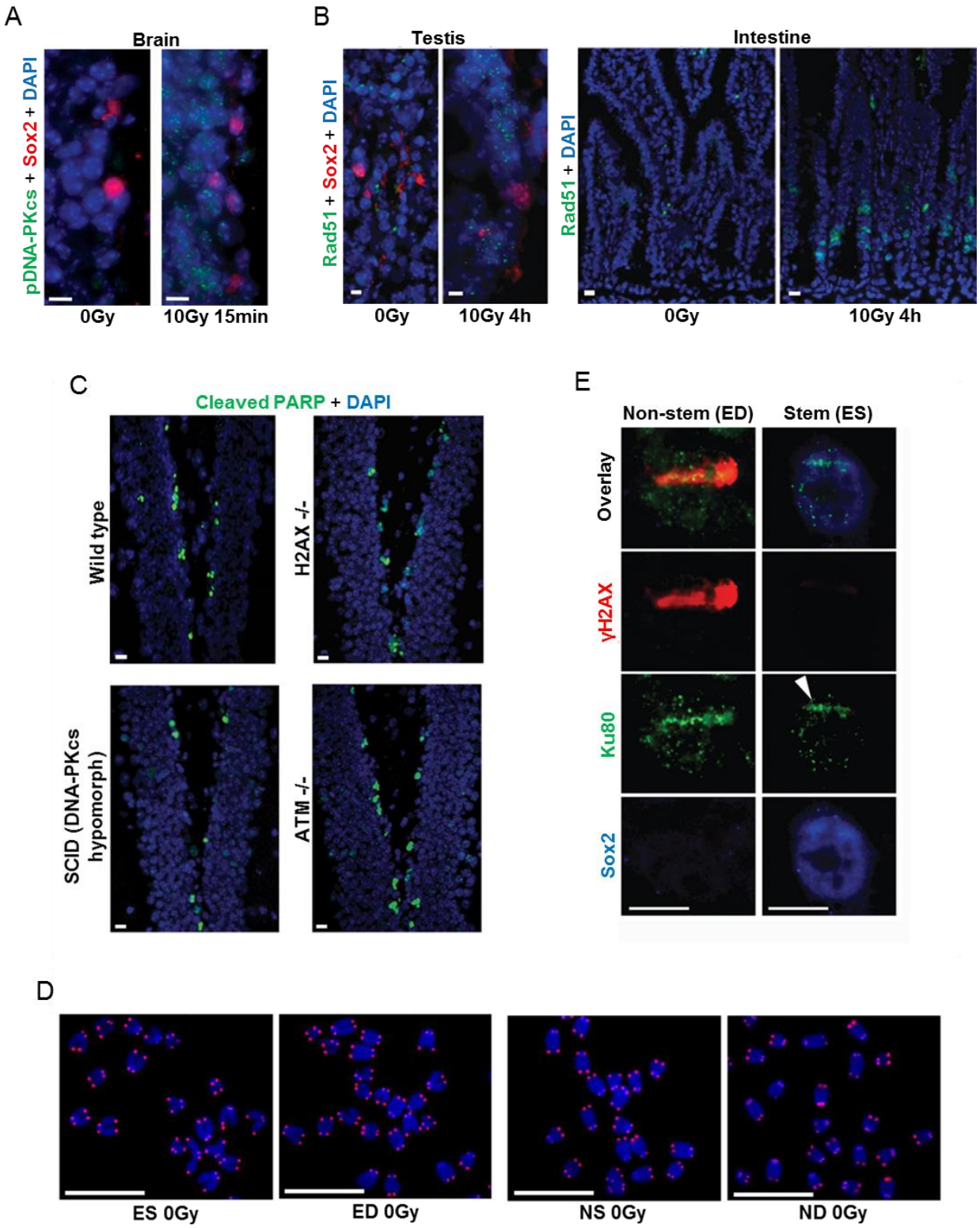

Supplementary Figure S4, related to Figures 2-3.

(A) Co-staining of Sox2 (red) and pDNA-PK (S2056, green) in brain 4h following sham or 6Gy IR. N=10 sections across 3 different mice. Magnification, 63x. (B) Co-staining of PLZF (red) and Rad51 (green) in testis, and Rad51 (green) in intestine 4h following sham or 6Gy IR. N=3 sections across 3 different mice. Magnification, 20x (testis 0Gy), 63x (testis 10Gy), 20x (intestine). (C) Staining of cleaved PARP in wild type, H2AX -/-, SCID, and ATM -/- brain 6h following 6Gy IR. N=12 sections across 3 mice each. Magnification, 20x. (D) Cytogenic analysis of chromosomes isolated from unirradiated ES, ED, NS and ND cells. Red, telomere. Over 100 chromosomes were imaged per sample, N=3 repetitions. Magnification, 100x. (E) Co-staining of Sox2 (blue), γH2AX (red) and Ku80 (green) on co-plated ES and ED cells following microirradiation, N=20. Magnification, 63x. DAPI=DNA. White scale bars, 10μm. Representative images are shown. Microirradiation results were consistently observed in at least 75% of experiments.

SUPPLEMENTARY FIGURE S5

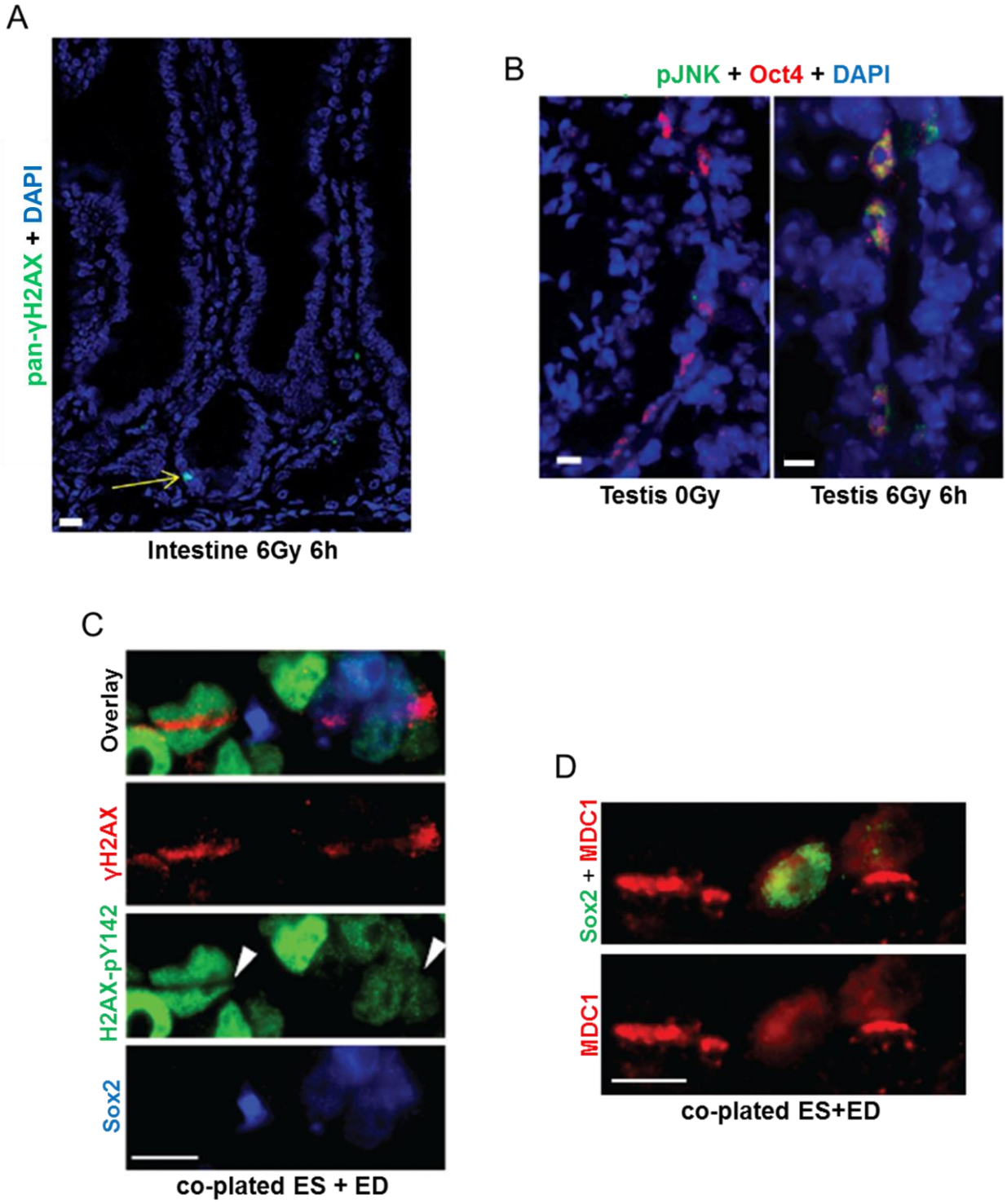

Supplementary Figure S5, related to Figure 4.

(A) Staining of pan-γH2AX (green) in intestinal crypt 6h following 6Gy IR. Arrows indicate apoptotic pan-γH2AX within the stem cell region. N=10 sections across 3 different mice. Magnification, 20x. (B) Co-staining of pJNK (T183/Y185, green) and Oct4 (red) in testis 6h following 6Gy IR. N=10 sections across 3 different mice. Magnification, 40x (left), 63x (right). (C) Co-staining of Sox2 (blue) H2AX-pY142 (green), and γH2AX (red) on co-plated ES and ED cells following microirradiation, N=25. White arrowheads indicate H2AX-pY142 dephosphorylation at γH2AX-labeled DNA breaks only in non-stem cells. Magnification, 63x. (D) Co-staining of MDC1 (red) and Sox2 (green) on co-plated ES and ED cells following microirradiation, N=10. Magnification, 63x. DAPI=DNA. White scale bars, 10μm. Representative images are shown. Microirradiation results were consistently observed in at least 75% of experiments.

SUPPLEMENTARY FIGURE S6

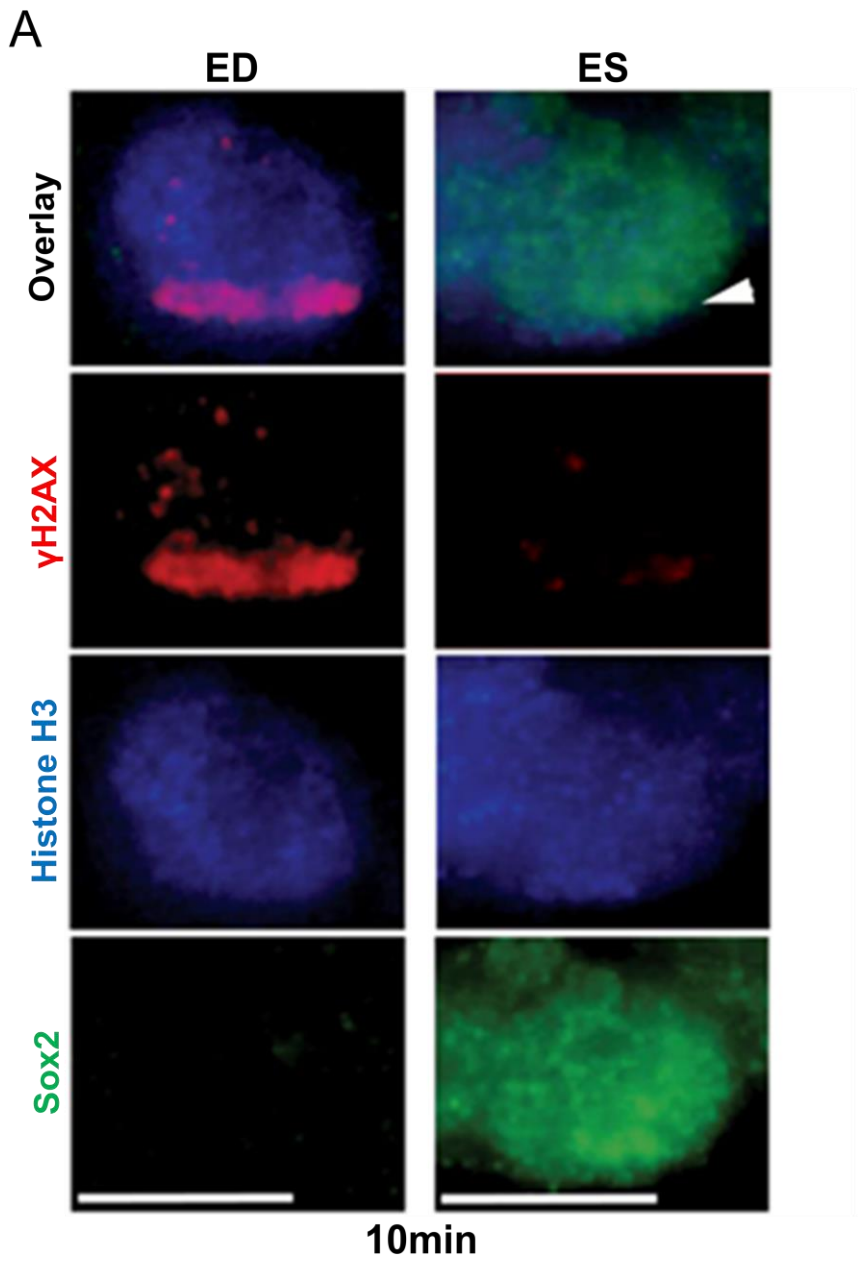

Supplementary Figure S6, related to Figure 6.

(A) Co-staining of Sox2 (green), γH2AX (red) and histone H3 (blue) on co-plated ES and ED cells 10min following microirradiation, N=15. Arrowhead marks the path of microirradiation across the stem cell. Magnification, 63x. White scale bars, 10μm. Representative images are shown. Microirradiation results were consistently observed in 100% of experiments.

SUPPLEMENTARY FIGURE S7

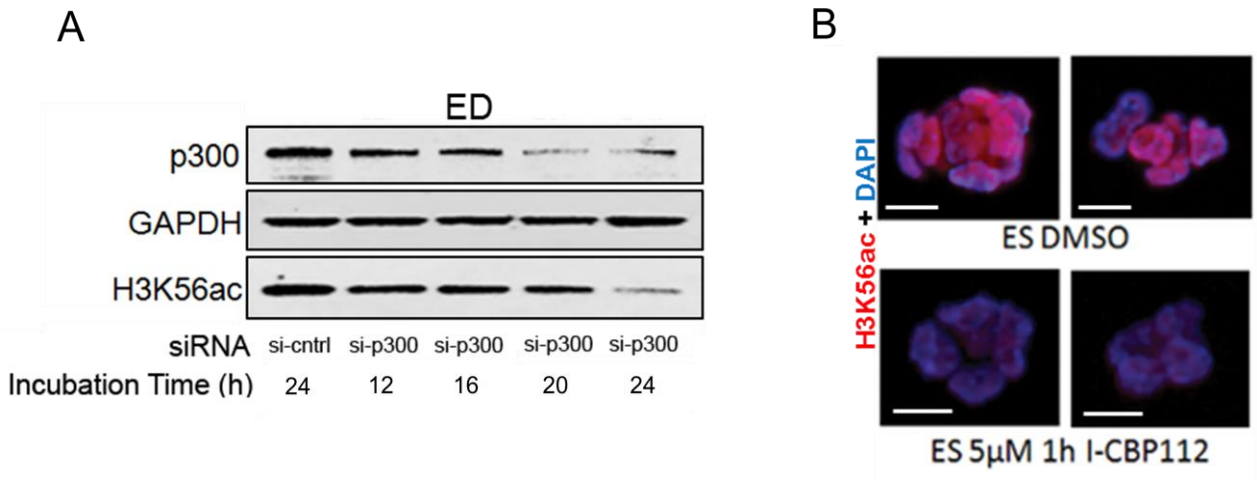

Supplementary Figure S7, related to Figure 7.

(A) Western blots for p300 and H3K56ac on ED cells following incubation for various timepoints with p300-targeted or control siRNA. (E) Staining of H3K56ac on ES cells following 1h incubation with DMSO or 5μM I-CBP112 inhibitor. GAPDH is loading control. DAPI=DNA. N=50 colonies, 3 repetitions. Magnification, 63x. White scale bars, 10μm. Representative images and blots are shown.

SUPPLEMENTARY TABLE S1 – List of antibodies used in this study

Protein Target	Species	Company	Catalog #	Assay	Conditions
Acetylated Histone H3	rabbit	Millipore	06-599	WB	1:2000 in BSA
Acetylated Histone H4	rabbit	Millipore	06-598	WB	1:1000 in BSA
Acetylated Histone 3 (K56)	rabbit	Millipore	04-1135	IF, IHC-F	1:250, 1:100
Bax	mouse	Santa Cruz	sc-7480	WB	1:250 in milk
Bcl2	rabbit	Cell Signaling	#2870	WB	1:100 in milk
BrdU (AlexaFluor 488 conjugated)	mouse	Invitrogen	B35139	FACS	1:20
Cleaved Caspase-3	rabbit	Cell Signaling	#9664	IHC-F, WB	1:500, 1:500 in milk
Cleaved PARP	mouse	BD Biosciences	51-9000017	IHC-F	1:100
Histone H2AX	rabbit	Cell Signaling	#7631	IF, WB	1:150, 1:2000 in BSA
Histone H3	rabbit	Cell Signaling	#4499	IF	1:250
Ku80	rabbit	Cell Signaling	#2753	IF	1:200
Lin28	rabbit	Abcam	ab46020	WB	1:1000 in milk
MDC1	mouse	Millipore	05-1572	IF	1:150
MST1	rabbit	Cell Signaling	#3682	IHC-F	1:50
Nanog	rabbit	Abcam	ab80892	WB	1:1000 in milk
NBS1	rabbit	Abcam	ab32074	IF	1:200
Oct4	rabbit	Abcam	ab19857	IF, IHC-F, WB	1:200, 1:200, 1:1000 in milk
p300	rabbit	Santa Cruz	Sc-585	WB	1:4000 in milk
PARP	rabbit	Cell Signaling	#9542	WB	1:2000 in milk
phospho-ATM (S1981)	mouse	Rockland	200-301-400	IF	1:200
phospho-ATM (S1981)	mouse	Cell Signaling	#4526	WB, IHC-F	1:500 in milk, 1:50
phospho-ATR (S1989)	rabbit	GeneTex	GTX128145	WB	1:1000 in BSA
phospho-Chk1 (S345)	rabbit	Cell Signaling	#2348	WB	1:1000 in BSA
phospho-DNA-PK (S2056)	rabbit	Abcam	ab18192	IF, IHC-F	1:200, 1:100
phospho-H2AX (Y142)	rabbit	Abcam	ab9045	IF, WB	1:200, 1:2000

phospho-JNK (T183/Y185)	mouse	Santa Cruz	sc-6254	IHC-F, WB	1:50, 1:500
phospho-MST1 (T183)	rabbit	Cell Signaling	#3681	WB	1:1000 in BSA
PLZF	mouse	Santa Cruz	sc-28319	IHC-F	1:50
Pro Caspase-3	rabbit	Cell Signaling	#9665	WB	1:1000
Rad51	rabbit	Santa Cruz	sc-8349	IHC-F	1:100
Sox2	rabbit	Abcam	ab7959	IHC-F, WB	1:100. 1:1000 in milk
Sox2	mouse	Abcam	ab79351	IF, IHC-F	1:200, 1:100
SSEA1	mouse	Abcam	ab16285	IHC-F, WB	1:100, 1:1000 in milk
Total ATM	rabbit	Cell Signaling	#2873	WB	1:1000 in BSA
Total ATR	rabbit	Cell Signaling	#2790	WB	1:500 in milk
Total Chk1	mouse	Cell Signaling	#2360	WB	1: 1000 in milk
γH2AX (S139)	mouse	Millipore	05-636	WB, IHC-F	1:4000 in BSA, 1:400
γH2AX (S139)	rabbit	Cell Signaling	#7631	IHC-F	1:150
GAPDH	mouse	Sigma Aldrich	G8795	WB	1:100,000 in milk
FITC-conjugated anti-rabbit	donkey	Vector	FI-1000	IF, IHC-F	1:100
FITC-conjugated anti-mouse	horse	Vector	FI-2000	IF, IHC-F	1:100
AMCA-conjugated anti-mouse	horse	Vector	CI-2000	IF	1:75
AMCA-conjugated anti-rabbit	donkey	Vector	CI-1000	IF	1:75
Texas Red-conjugated anti-mouse	horse	Vector	TI-2000	IF, IHC-F	1:100
Texas Red-conjugated anti-rabbit	donkey	Vector	TI-1000	IF, IHC-F	1:100
HRP-conjugated anti-mouse	rabbit	Sigma Aldrich	A9044	WB	1:5000 in milk
HRP-conjugated anti-rabbit	goat	Sigma Aldrich	A0545	WB	1:5000 in milk

SUPPLEMENTAL TABLE S2 – siRNA sequences

siGENOME Non-Targeting siRNA Pool #1	siGENOME SMARTpool EP300 siRNA
UAGCGACUAAACACAUCAA	CGAGAGUACUGAUGUAACA
UAAGGCUAUGAAGAGAUAC	CGGCAUGCAUGUUCAAGAA
AUGUAUUGGCCUGUAUUAG	CAAGAGCCCUGGCAAUAUA
AUGAACGUGAAUUGCUCAA	GGACUACCCUAUCAAGUAA